J. Fluid Mech. (2002), *vol.* 460, *pp.* 93–129. © 2002 Cambridge University Press
DOI: 10.1017/S0022112002008133 Printed in the United Kingdom

Wave interaction with a vertical cylinder: spanwise flow patterns and loading

By Y. YANG† AND D. ROCKWELL

Department of Mechanical Engineering and Mechanics, 354 Packard Laboratory, 19 Memorial Drive West, Lehigh University, Bethlehem, PA 18015, USA

(Received 5 January 2001 and in revised form 14 November 2001)

A vertical cylinder is located in a free-surface wave, and a two-camera version of high-image-density particle image velocimetry is employed to characterize the spanwise modes of the flow structure in terms of instantaneous velocity and vorticity. These modes are classified according to organized patterns of velocity in the near wake, and are further interpreted in terms of distinctive arrangements of streamwise vorticity concentrations.

At low Keulegan–Carpenter number, which corresponds to small wave height, locally two-dimensional vortices having small scale and circulation tend to form as a symmetrical pair and remain attached, or in close proximity, to the surface of the cylinder. Along the span of the cylinder, the near wake shows either a sinuous S or a unidirectional U mode. The spanwise wavelength λ of the S modes, relative to the cylinder diameter D, lies in the range $1 \lesssim \lambda/D \lesssim 4.5$. These values of λ/D represent the spacing between extrema of patterns of crossflow velocity, as well as between clusters of streamwise vorticity of like sign. As the free surface is approached, the value of λ/D scales with the ratio of the minor to major axes of the elliptical particle trajectory of the wave.

At moderate values of the Keulegan–Carpenter number, locally two-dimensional vortices having large scale and circulation are shed from the cylinder in an asymmetric arrangement. The corresponding spanwise mode represents the phase variation of this shedding along the span of the cylinder. These sinuous S modes involve large-scale distortions of patterns of both crossflow velocity and streamwise vorticity, which have wavelengths in the range $10 \lesssim \lambda/D \lesssim 110$, in contrast to the spacing between individual concentrations of vorticity, which is $1.5D$ to $4D$. Remarkably, it is possible to attain a unidirectional U mode, whereby the phase of the locally two-dimensional vortex shedding is preserved along the entire extent of the cylinder.

Signatures of the moments due to the transverse and in-line forces on the cylinder were acquired simultaneously with the patterns of instantaneous velocity and vorticity. Severe modulations of the moment due to the transverse force are associated with spontaneous transformations between basic forms of the sinuous S and unidirectional U modes. The overall form of the signature of the moment due to the in-line force is, however, not generally affected by the spontaneous transformation between modes, but distortion of its peaks is evident.

---

† On leave from Beijing Institute of Aerodynamics (BIA).

https://doi.org/10.1017/S0022112002008133 Published online by Cambridge University Press

1. Introduction

Loading of cylindrical structures in ocean and coastal engineering applications is of continuing importance. Risers, cables and related configurations are subjected to wave motion and may undergo undesirable vibration. Over the years, substantial efforts on experimental, numerical and theoretical fronts have addressed the central issues of this class of problems.

Simulation of loading due to long waves can be accomplished by subjecting a stationary cylinder to unidirectional oscillatory flow or, conversely, oscillating a cylinder in quiescent fluid. The classes of quasi-two-dimensional modes of vortex formation from the cylinder, as well as the magnitudes of the in-line and transverse forces, are a function of the Keulegan–Carpenter number $KC = 2\pi A_0/D$, in which A_0 is the displacement amplitude of the oscillatory flow or cylinder motion and D is the diameter, as well as the Stokes number $\beta = fD^2/\nu$, in which f is the frequency of the motion and ν is the kinematic viscosity. The investigations of Singh (1979), Bearman *et al.* (1981), Sarpkaya & Isaacson (1981), Ikeda & Yamamoto (1981), Iwagaki, Asano & Nagai (1983), Williamson (1985), Obasaju, Bearman & Graham (1988), Dütsch *et al.* (1998*a*) and Lin & Rockwell (1999) characterized, in either a qualitative or quantitative fashion, the modes of quasi-two-dimensional vortex formation in relation to the loading on the cylinder.

For the case of a vertical cylinder in a wave, the axis of the orbital particle trajectory of the incident wave is orthogonal to the axis of the cylinder and one expects the loading to show distinctive features relative to the case of a horizontal cylinder beneath a wave. The loading on vertical cylinders has been addressed by Ramberg & Niedzwecki (1979), Chakrabarti (1980), Stansby, Bullock & Short (1983), Bearman *et al.* (1985) and Tørum (1989). In addition, Sarpkaya (1984) simulated a vertical cylinder in a wave by imparting vertical motion to a cylinder in a unidirectional oscillatory flow. A field experiment was described by Dean, Dalrymple & Hudspeth (1981). Sumer & Fredsøe (1997) gave an assessment of the loading of vertical cylinders in waves in comparison with loading in a unidirectional oscillatory flow.

For the foregoing categories of oscillating flow–cylinder and wave–cylinder interaction, one expects the existence of three-dimensionality, at least to a degree, along the span of the cylinder. In fact, the spanwise correlation coefficients of fluctuating pressure of Obasaju *et al.* (1988) and Kozakiewicz, Sumer & Fredsøe (1992) clearly indicate that the loading on a cylinder immersed in a unidirectional oscillatory flow is three-dimensional. The decay of the correlation coefficient along the span of the cylinder is a strong function of the Keulegan–Carpenter number KC. Furthermore, Obasaju *et al.* (1988) visualized the vortex modes in two different planes orthogonal to the axis of the cylinder. The difference between these modes indicated three-dimensionality along the span.

Honji (1981) discovered highly organized, three-dimensional modes having a spanwise wavelength λ, relative to the cylinder diameter D, of the order of $\lambda/D = 0.5$ to 1.0, for the case of an oscillating cylinder in quiescent water. Sarpkaya (1986) provided further insight into the Honji instability, including its inception and the onset of separation and turbulence on an oscillating cylinder. Tatsuno & Bearman (1990) classified the modes of three-dimensionality along the span of the cylinder as a function of the Keulegan–Carpenter number KC and the Stokes number β. Depending upon the particular regime observed, the spanwise wavelengths ranged from $\lambda/D \approx 0.8$ to 6.0. Dütsch, Durst & Brenner (1998*b*) and Dütsch (2000) performed a numerical simulation of the three-dimensional modes induced by an oscillating

https://doi.org/10.1017/S0022112002008133 Published online by Cambridge University Press

circular cylinder at low KC and Reynolds number Re. The flow structure illustrated in their visualization exhibits a spanwise periodicity of the order of $\lambda/D \approx 2.5$. Most recently, Elston, Blackburn & Sheridan (2000) employed a Floquet analysis in conjunction with a direct numerical simulation to calculate the three-dimensional modes. Depending upon the value of KC and β, highly ordered spanwise patterns of vorticity having a spanwise wavelength $\lambda/D = 1.4$ to 3.9 were observed.

The focus of the present investigation is on the three-dimensionality of the near wake of a vertical cylinder piercing a free-surface wave, and its relation to the loading of the cylinder. In contrast to the case of unidirectional oscillatory flow past a stationary cylinder or, conversely, oscillation of the cylinder in quiescent fluid, the interaction of a wave with a vertical cylinder is inherently more complex. The axis of the elliptical particle trajectory of the wave motion is orthogonal to the axis of the cylinder. Depending on the type of wave, the ratio of the minor to major axes of the elliptical motion may be a function of depth. Furthermore, the end conditions involve an oscillatory free-surface condition at the upper end and a solid boundary condition at the bottom end. The admissible modes of three-dimensional vortex formation along the span of the cylinder and their relation to the cylinder loading are unknown. An intriguing possibility is attaining spanwise modes and loading that are highly correlated, i.e. unidirectional, even in the presence of the spanwise variations of the characteristics of the incident wave.

The aim of the present study is to address the foregoing issues using patterns of instantaneous velocity and vorticity along the span of the cylinder. A technique of high-image-density particle image velocimetry is employed, and the instantaneous images are correlated with instantaneous values of the moments due to the transverse and in-line forces, in order to determine the degree to which the three-dimensionality influences the loading.

2. Experimental system and techniques

2.1. *Wave tank-cylinder system*

Experiments were performed in a custom-designed wave tank in order to allow three-dimensional illumination and imaging of flow modes. Selected aspects of this facility, as well as a representative image, are described by Rockwell *et al.* (2001). Figure 1(*a*) shows an overview of the wave tank. It had a width of 426 mm, a depth of 1018 mm and a length of 9300 mm. Water was maintained at a nominal depth of 700 mm. Waves were generated by a paddle-type wave generator with active control via force feedback (Edinburgh Designs, Ltd.). A 1270 mm long wedge (included angle of 19°) of absorbent porous material was located at the other end of the wave tank.

A cylinder of diameter $D = 12.7$ mm and length $L = 876$ mm was employed, and the length of the submerged part of the cylinder was 700 mm. At the given wave frequency $f = 0.5$ Hz, values of Keulegan–Carpenter number $KC = 2\pi A_0/D = 4.5$ to 21.4 were generated by variation of the paddle amplitude. In this definition of KC, A_0 is the horizontal displacement amplitude of the wave, i.e. half the major axis A of the orbital particle trajectory of the wave, and D is the diameter of the cylinder. Unless otherwise indicated, the reference value of A_0 is always evaluated at the free surface. Over this range of KC, the wave amplitude varied from 3.2 to 22.6 mm. The value of the Stokes number was $\beta = fD^2/\nu = 73$ for all experiments.

https://doi.org/10.1017/S0022112002008133 Published online by Cambridge University Press

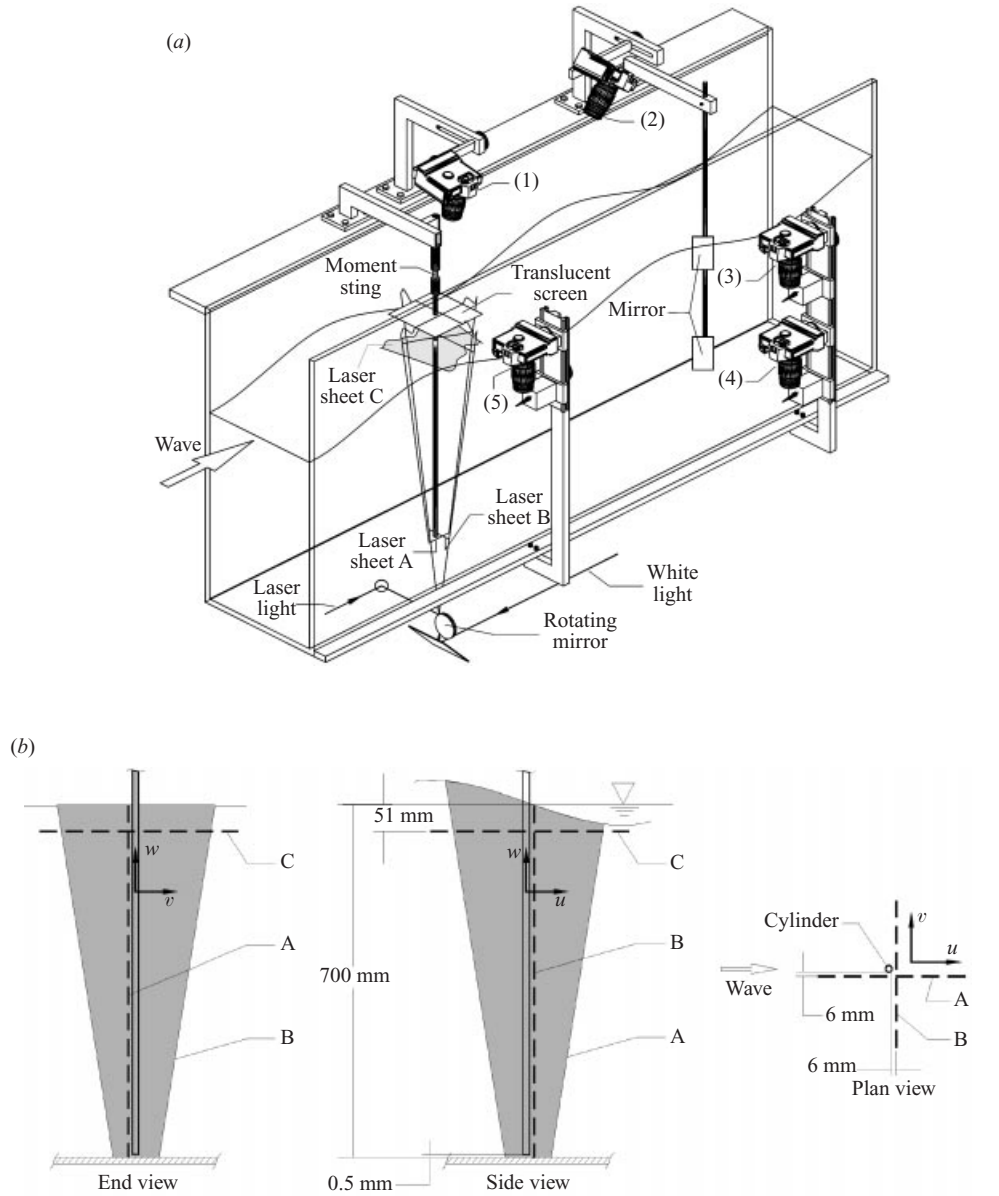


FIGURE 1. (*a*) Schematic of the experimental system illustrating the wave tank, laser sheets, and orientations and arrangements of cameras employed for high-image-density particle image velocimetry, laser-induced qualitative visualization and shadowgraph techniques. (*b*) Schematic showing illustrations of laser sheet A, which is oriented in the wave direction, laser sheet B, which is orthogonal to the wave, and sheet C, which is parallel to the still free surface. Also shown are definitions of the velocity components.

2.2. *Wave characterization*

The aim of this investigation is to investigate wave–cylinder interaction for the case where the ratio of the minor axis B to the major axis A of the orbital particle trajectory of the wave exhibits large variations with depth. This goal is accomplished by the generation of a wave with an elliptical particle trajectory at the free surface and

https://doi.org/10.1017/S0022112002008133 Published online by Cambridge University Press

a unidirectional trajectory at the bottom of the wave tank. The wave had a frequency $f = 0.5\,\mathrm{Hz}$ and the nominal water depth was $d = 700\,\mathrm{mm}$. The corresponding wavelength of the free-surface wave was $\lambda = 4620\,\mathrm{mm}$, which corresponds to a value of $kd = 2\pi d/\lambda = 0.95$. This means that the wave is intermediate between the long-wave and deep-water limits.

During preliminary experiments, it was found that even a small ratio of the reflected to incident wave energy could significantly distort the particle trajectories of the wave motion. Placement of the vertical cylinder at the minimum amplitude of the wave system provides two advantages. First, at this location, the major axes A of the particle orbits at all values of depth are oriented in the horizontal direction; away from this location, the major axes are inclined with respect to the horizontal (Ippen 1966). Second, the variation with depth of the minor B and major A axes of the orbital trajectories corresponds to that of the classical intermediate wave (Ippen 1966; Lighthill 1978). In essence, the axes A and B are proportional to $\cosh k(d+z)$ and $\sinh k(d+z)$ respectively. The orbital particle trajectories at each value of KC were determined experimentally using the technique of high-image-density particle image velocimetry (PIV). The Keulegan–Carpenter number of the wave system is defined as $KC = 2\pi A_0/D$, in which $A_0 = A/2$ is the amplitude of the horizontal displacement of the orbital trajectory of the wave at the free surface. This PIV technique, in conjunction with the aforementioned analysis of Ippen (1966), also allowed determination of the ratio of the reflected to incident wave energy, i.e. $E_r/E_i = 13.7\%$, 6.2% and 3.5% at values of $KC = 4.5$, 10 and 18.

Figure 2 shows the characteristics of the wave at the location of the cylinder, but in its absence. Figure 2(*a*) compares the theoretical orbital trajectories at selected depths beneath the free surface, obtained from Ippen (1966), with those determined experimentally using the PIV technique for a representative value of $KC = 17$. Figure 2(*b*) shows the ratio of the minor B axis to the major A axis of the elliptical trajectory at the free surface as a function of KC. Figure 2(*c*) exhibits the ratio B/A normalized by the free surface value $(B/A)_0$ as a function of both depth z beneath the free surface and depth normalized by the cylinder diameter, z/D; this variation is universal for all KC. It is evident that the flow is orbital at the free surface and unidirectional at the bottom of the tank. Finally, figure 2(*d*) shows the variation of the major axis A of the orbital trajectory normalized by D as a function of depth for three values of KC. Taken together, figures 2(*c*) and 2(*d*) show that B/A undergoes a large change from the free surface to the bottom of the wave tank, while KC decreases by 33%.

2.3. *Ranges of parameters: physical basis*

In order to determine the most appropriate values of Keulegan–Carpenter number $KC = 2\pi A_0/D$ and Stokes number $\beta = fD^2/\nu$, and thereby values of Reynolds number $Re = KC\beta$, the series of investigations described in the Introduction were employed as a guide. More specifically, experimental flow visualization and numerical simulation of the patterns of vortex formation for unidirectional oscillatory flow past a stationary cylinder and oscillatory motion of a cylinder in quiescent fluid served as a framework for selection of parameters of the actual wave–cylinder interaction of interest in the present study.

Low Keulegan–Carpenter number. At and below the representative low value of $KC = 4.5$ selected for the present study, small-scale vortices form during the initial phase of unidirectional, oscillatory motion, and they remain attached, or in close proximity, to the cylinder. In fact, the initially formed vortices resemble the sym-

https://doi.org/10.1017/S0022112002008133 Published online by Cambridge University Press

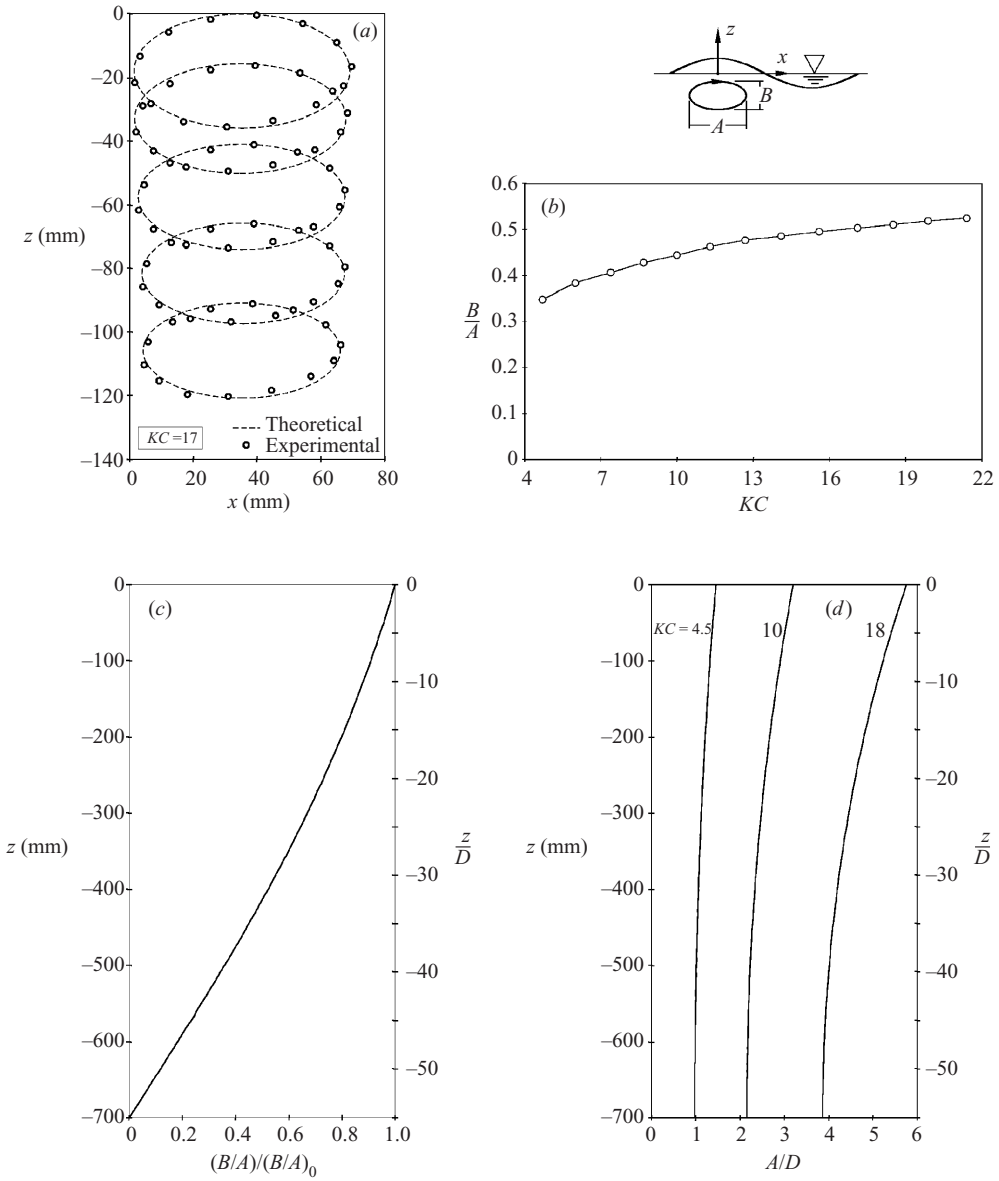


FIGURE 2. (*a*) Experimental and theoretical particle trajectories of the surface wave; (*b*) variation of the ratio of the minor B axis to the major A axis of the ellipse as a function of Keulegan–Carpenter number KC; (*c*) variation of B/A, normalized by free-surface value $(B/A)_0$ with depth z; and (*d*) amplitude A of the ellipse normalized by the cylinder diameter D as a function of depth (z) beneath the free surface.

metrical vortex pair from an abruptly accelerated cylinder. This type of pattern has been observed at values of KC close to or at 4.5 for $\beta = 20$ (Dütsch *et al.* 1998*a*), $\beta = 45.2$ (Tatsuno & Bearman 1990), and $\beta = 730$ (Williamson 1985). Regarding the symmetry of the initially formed vortex pair, Williamson (1985) found that above $KC = 4$, the attached, nominally symmetrical vortices may exhibit unequal strength. Since the value of $KC = 4.5$ at the free surface decreases with depth, this pattern

https://doi.org/10.1017/S0022112002008133 Published online by Cambridge University Press

of near-wake vortex formation remains similar with depth, i.e. the formation of an attached vortex pair of ever decreasing scale.

Intermediate Keulegan–Carpenter number. An intermediate value of $KC = 10$ corresponds to the occurrence of shed, as opposed to attached, vortices in the near wake. During the initial phase of the oscillatory motion, Kármán-like shedding of a large-scale vortex appears in the near wake. This basic pattern is evident at or near $KC = 10$ for $\beta = 20$ (Dütsch *et al.* 1998*a*), $\beta = 37.7$ (Tatsuno & Bearman 1990), $\beta = 416$ (Obasaju *et al.* 1988), and $\beta = 730$ (Williamson 1985). For the present case of the wave, the value of $KC = 10$ at the free surface decreases to $KC = 6.7$ at the floor of the wave tank. As indicated by Williamson (1985), the basic pattern of quasi-two-dimensional, large-scale vortex formation has the same form over this range of KC. Finally, the intermediate range of KC of the present investigation also includes $KC = 18$ at the free surface, which decreases to $KC = 12.1$ at the bottom of the wave tank. For unidirectional oscillatory motion, the initial phase of shedding of the large-scale vortex in the near wake at $KC = 18$ is similar to that at $KC = 10$ as indicated by regimes in Williamson (1985), the subsequent details of additional vortex formation and interaction notwithstanding. It is this initial phase that is of primary interest in the present investigation, which focuses on definition of the spanwise modes in the near wake.

Stokes number. The value of $\beta = fD^2/\nu$ for the present experiment was defined on the basis of the anticipated three-dimensional structure along the span of the cylinder. Tatsuno & Bearman (1990) provided a detailed regime map of three-dimensional states on a plane of KC versus β for the case of an oscillating cylinder in quiescent fluid. At a low value of $\beta \lesssim 55$, a multiplicity of complex, three-dimensional states can occur as KC increases from 0 to 10. On the other hand, at a sufficiently high value of, for example, $\beta = 73$, which was selected for the present study, a simpler set of three sequential, three-dimensional states (designated as a states B, E, and G) occurs as KC increases. The aforementioned values of KC of the present study extend over these three states. All of the visualization photos of Tatsuno & Bearman (1990), as well as values of measured wavelength λ/D of the spanwise three-dimensionality, are, however, for values of β lower than 73. In their study, turbulent motion appeared when β was sufficiently large, and although the flow was anticipated to have a three-dimensional structure, it did not appear to be regular along the cylinder axis. This difficulty in defining the three-dimensional flow structure is no doubt due to the relatively high value of $Re = KC\beta$ and the associated challenges of interpreting patterns of the visualization marker. The present investigation focuses on this higher range of Re and aims to define the admissible modes of the three-dimensionality.

2.4. *Visualization: shadowgraph and quantitative imaging techniques*

The overview of figure 1(*a*) shows the illumination and image recording systems in relation to an isometric schematic of the wave tank. Shadowgraph visualization involved use of a translucent screen oriented horizontally and positioned at an elevation of 80 mm above the nominal elevation of the free surface. The white light illumination for the shadowgraph originated from a 35 mm projector system. As indicated at the bottom of the schematic, this white light was reflected from a mirror located beneath the tank. Images on the shadowgraph screen were recorded using a film-based camera (1).

As shown in figure 1(*a*) and in further detail in figure 1(*b*), the characteristics of the unsteady wave system and its interaction with the cylinder were visualized using laser sheets A and B, which provided side and end views respectively of the

https://doi.org/10.1017/S0022112002008133 Published online by Cambridge University Press

instantaneous flow mode. These laser sheets were located a distance of 6 mm from the surface of the cylinder. Two types of visualization were performed using laser sheet B. The first involved illumination of the microbial growth suspended in water that was untreated for two days. For this purpose, camera (2) was employed. The visualized flow pattern was entirely qualitative. Quantitative representations of the spanwise modes in laser sheet B were obtained via a technique of high-image-density particle image velocimetry. Multiply-exposed images of metallic-coated 14 micron diameter spheres in clean water were reflected from two small (64 mm × 114 mm) mirrors located within the wave and at a distance of 1170 mm from laser sheet B. The images were recorded using two film-based camera–bias mirror systems designated as (3) and (4); these systems were synchronized using a microcomputer. Images obtained in laser sheet A, corresponding to a side view, were recorded using camera (5) and its associated bias mirror.

In order to generate laser sheets A and B, the beam from a 20 W continuous argon-ion laser was reflected from a rotating mirror having 48 facets. This mirror was located beneath the tank, as indicated in the schematic. The effective scanning frequency generated by the rotating mirror depended upon the value of the Keulegan–Carpenter number $KC = 2\pi A_0/D$. For laser sheet B, at $KC = 10$, it was 55 Hz, and at $KC = 18$, it was 106 Hz. For the smallest value of $KC = 4.5$, an oscillating mirror was employed; it was driven by a galvanometer scanner at 20 Hz. For the side view of laser sheet A, which was used to determine the orbital particle trajectories of the wave, the rotating mirror was employed; at $KC = 17$, the scanning frequency was 135 Hz. The scanning beam illuminated hollow plastic spheres, which were metallic coated. The spherical particles had a nominal diameter of 14 microns. These particles were dispersed throughout the wave tank, and the water was allowed to attain a quiescent state, prior to initiation of the wavemaker.

For the images acquired in the end view of laser sheet B, corresponding to cameras (3) and (4) in figure 1(*a*), a magnification of 1 : 11 was employed. This provided a field of view for each of the cameras of 264 mm × 396 mm in the plane of the laser sheet. High-resolution film was employed in both cameras (3) and (4). It had a resolution of 300 lines mm^{-1} and was digitized at a resolution of 125 pixels mm^{-1}. A single-frame cross-correlation technique was employed to evaluate the velocity field. The size of the interrogation window was 90 pixels × 90 pixels. Successive interrogation windows overlapped by 50%. The effective grid size was 4 mm. Moreover, each interrogation window contained approximately 40 particle images. The procedure and parameters for recording images in the side view of laser sheet A by camera (5) were the same as those for the end view, except as follows. The effective field of view was 118 mm × 177 mm. The value of magnification was 1 : 4.9, leading to an effective grid size of 1.8 mm.

A technique of digital particle image velocimetry (DPIV) was used to supplement the film-based PIV, which was the primary method of this investigation. For the DPIV approach, laser illumination was provided from a 90 mJ dual-pulsed Yag laser system. The laser sheet was transmitted through a cylindrical lens, then directly through the sidewall of the wave tank to form laser sheet B. Images were recorded using a digital camera having a resolution of 1000 pixels × 1016 pixels. Instantaneous modes of velocity were evaluated using a frame-to-frame correlation technique. The field of view was 133 mm × 135 mm in the plane of the laser sheet. During the interrogation process, an effective window size of 32 pixels × 32 pixels was employed, with an overlap of 50%. The effective grid size was therefore 2.1 mm.

DPIV was also employed to characterize the modes of locally two-dimensional

https://doi.org/10.1017/S0022112002008133 Published online by Cambridge University Press

vortex shedding beneath the free surface, relative to the shadowgraph visualization of the free surface distortion. Laser sheet C, indicated by the shaded region in figure 1(*a*) and shown in further detail in figure 1(*b*), was employed for this purpose. It was located a distance of 51 mm beneath the undisturbed free surface. At the lowest value of $KC = 4.5$, the field of view was 59 mm × 60 mm in the plane of the laser sheet. At values of $KC = 10$ and 18, the view was 110 mm × 111 mm. For all interrogation processes, an effective window size of 32 pixels × 32 pixels was employed, also with 50% overlap, and the effective grid size in the plane of the laser sheet was 0.95 mm for $KC = 4.5$ and 1.75 mm for $KC = 10$ and 18.

2.5. *Measurements of cylinder loading*

The moments due to the in-line (x) and transverse (y) forces acting on the cylinder were determined using a high-sensitivity strain gauge system. The centre of the strain gauge system was 16.5D (210 mm) above the quiescent free surface. The outputs from the strain gauge amplifiers were transmitted to the laboratory microcomputer where they were recorded in synchronization with the wave motion. Values of the moment coefficients C_x^* and C_y^* due to the in-line and transverse forces are defined using the magnitude U of the horizontal velocity fluctuation at the mid-depth location of the wave tank. That is, measured values of moment were normalized by $(1/2)\rho U^2 D L^2$, where D and L represent the diameter and submerged length of the cylinder respectively.

3. Locally two-dimensional modes of vortex formation

3.1. *Images via shadowgraph visualization at the free surface*

Figure 3 shows a time sequence of shadowgraph images obtained at $KC = 10$ and 18. At these values, the strength of the shed vortices was large enough to produce well-defined images. At the lower limit of $KC = 4.5$ considered in this investigation, such well-defined modes were not attainable, and therefore are not represented in figure 3.

As indicated in the schematic at the upper right of the first shadowgraph image, the coordinate system looking down on the free-surface is (x, y); it is centred at the axis of the cylinder. The schematic at the lower right of each shadowgraph image indicates the instantaneous position (white dot) on the orbital trajectory of the incident wave; this orbit is in the (x, z)-plane.

Consider the shadowgraph images at $KC = 10$. The first image shows a black concentration A, which represents a vortex shed from the previous half-cycle of oscillation. In subsequent images, it forms a counter-rotating vortex pair with B, which is shed from the cylinder during the present half wave cycle. This mode is a well-known feature of vortex formation from cylinders in unidirectional oscillatory flow, as summarized by Sarpkaya & Isaacson (1981) and described, for example, by Williamson (1985), and Obasaju *et al.* (1988). In addition, this basic mode has been verified via quantitative PIV images for the equivalent scenario of an oscillating cylinder in quiescent fluid by Lin & Rockwell (1999). An analogous, but somewhat more complex mode of vortex formation is shown at $KC = 18$. It is also addressed in the foregoing references.

3.2. *Quantitative images beneath free surface*

Instantaneous patterns of velocity were acquired in a plane corresponding to the horizontal laser sheet C indicated in figure 1(*a*). It was located a distance of 4D =

https://doi.org/10.1017/S0022112002008133 Published online by Cambridge University Press

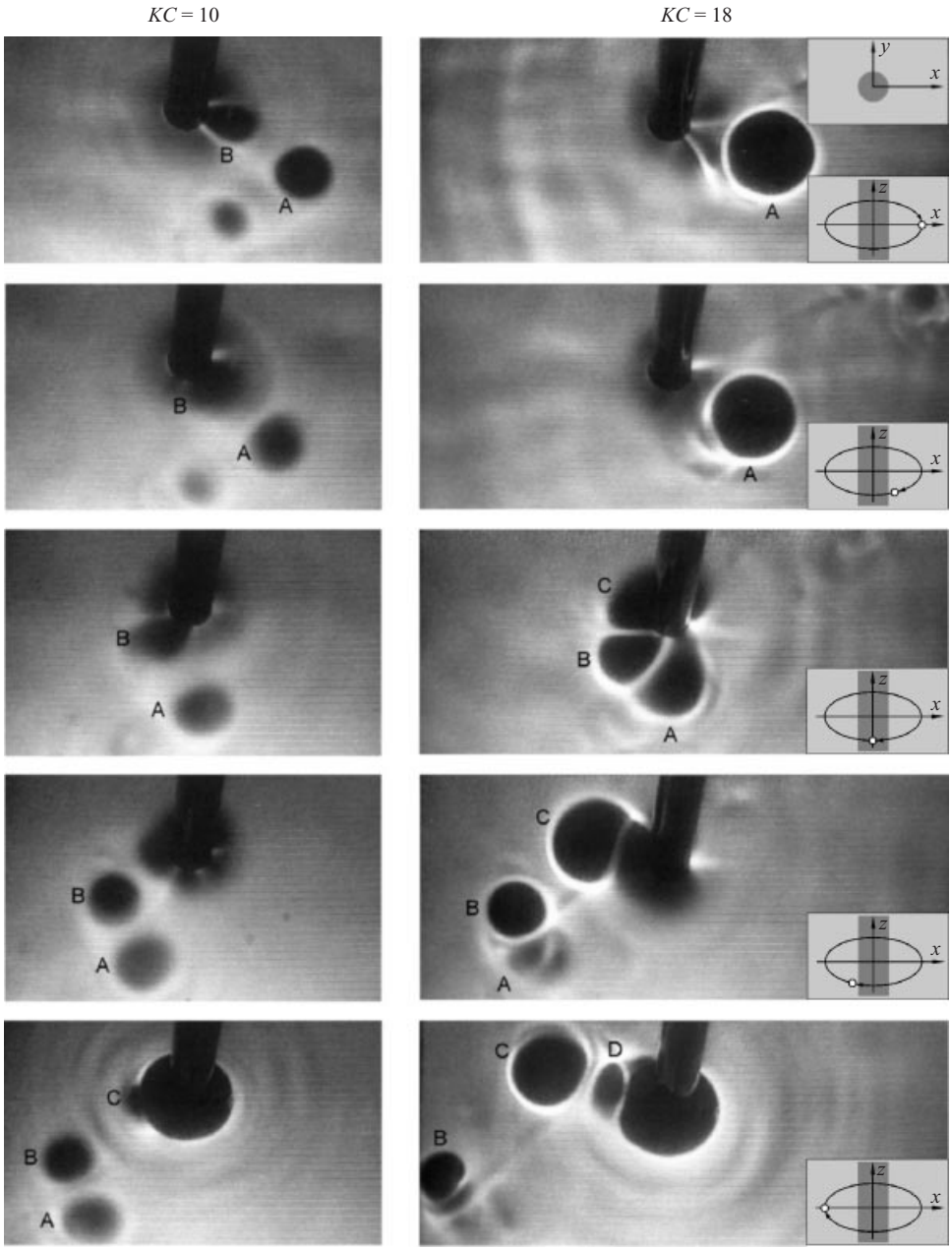


FIGURE 3. Shadowgraph visualization of vortex formation from the vertical stationary cylinder for $KC = 10$ and 18. Coordinates x, y define the horizontal plane and z, x the vertical plane.

51 mm beneath the quiescent free surface. These images are illustrated for three different values of KC in figure 4. All images were acquired at the same instant, i.e. phase, of the wave motion. It corresponded to a position midway between the trough and crest of the wave at the location of the cylinder.

At the low value of $KC = 4.5$, shown in image (i), the incipient state of vortex formation occurs symmetrically, whereas in image (ii), the initially formed vortex pair

https://doi.org/10.1017/S0022112002008133 Published online by Cambridge University Press

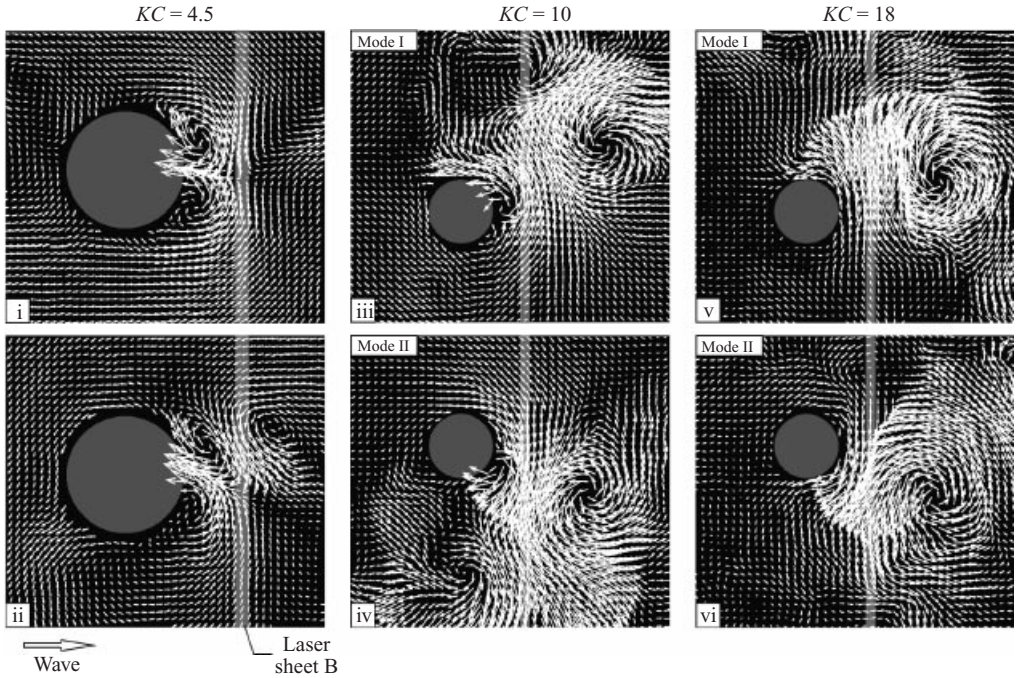


FIGURE 4. Patterns of instantaneous velocity acquired in a horizontal plane corresponding to laser sheet C designated in figure 1. For purposes of reference in subsequent figures, the location of vertical laser sheet B is designated by the thick grey line. All images were acquired at the same phase of the wave motion, corresponding to the position of the wave midway between its trough and crest at the location of the cylinder. At each value of KC, two admissible modes of vortex formation are shown, and at $KC = 10$ and 18, the modes are mirror images of one another; mode II at these values of KC can be compared with the top row of shadowgraph visualizations in figure 3.

shows a degree of asymmetry; an additional vortex, formed earlier, is also evident. Irrespective of the particulars of the vortex patterns in images (i) and (ii), all of the small-scale vortices remain attached, or in close proximity, to the cylinder. The dimensionless circulation of a given vortex is $\Gamma^* = \Gamma/UDKC$. It is normalized by the local horizontal velocity amplitude U, local Keulegan–Carpenter number KC, and the cylinder diameter D. The value of Γ was determined from corresponding patterns of vorticity. For the aforementioned vortices, $|\Gamma^*| = 0.12$ to 0.16, which is relatively small compared to the values of larger KC, as discussed below.

At the intermediate value of $KC = 10$, two distinct modes, designated I and II are evident. They are shown in images (iii) and (iv). Both modes indicate large-scale vortex formation in the near wake region, and modes I and II are mirror images of each other. Similarly, mirror-image modes I and II are given in images (v) and (vi) for $KC = 18$. The values of dimensionless circulation are in the range $|\Gamma^*| = 0.18$ to 0.39 for the shed vortices at the right of each image. At both $KC = 10$ and 18, the mirror-image modes of vortex formation show opposite directions of transverse velocity v in the plane of the laser sheet. This correspondence between the directions of velocity v and the occurrence of mode I or II is employed to interpret the modes of three-dimensional flow structure along the span of the cylinder, as addressed subsequently.

Bearman, Graham & Obasaju (1984) reported the occurrence of mirror-image modes on the basis of qualitative visualization. For the case of unidirectional flow past a stationary cylinder, they found that a given mode could transform to its mirror

https://doi.org/10.1017/S0022112002008133 Published online by Cambridge University Press

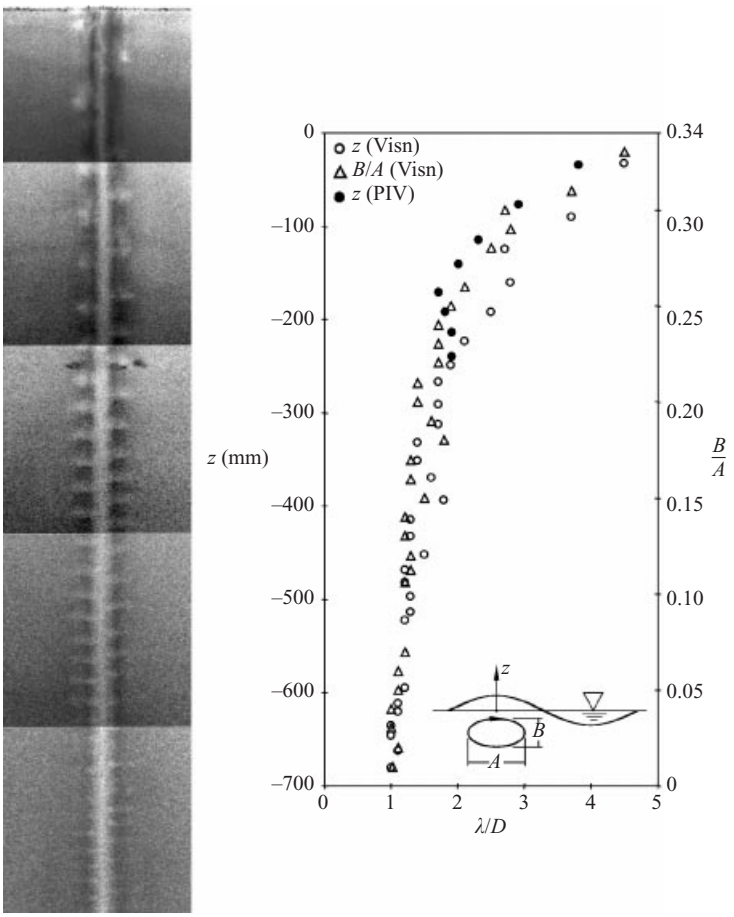


FIGURE 5. Visualization of the three-dimensional instability and plots of the variation of the wavelength λ/D of the instability as a function of depth z and the ratio of minor B to major A axis of the particle orbit of the wave. Data points are obtained from either visualization (Visn) or particle image velocimetry (PIV). The value of Keulegan–Carpenter number at the free surface is 4.5.

image at a given spanwise location. Switching between modes was addressed in detail by Obasaju *et al.* (1988), who employed a pointwise measurement technique on a given cross-sectional plane along the span of a stationary cylinder in a unidirectional oscillatory flow. Mode switching therefore appears to be an inherent feature of this class of flows. The issue therefore arises as to whether switches between modes on a given plane of observation are associated with transformations between instantaneous modes of three-dimensionality along the span of the cylinder. The present investigation addresses this aspect.

4. Small-scale spanwise modes

4.1. *Qualitative visualization*

Figure 5 shows qualitative visualization obtained using the end view defined by laser sheet B in figures 1(*a*) and 1(*b*). Rather than artificially seeding filtered water in the wave tank, microbial growth was allowed to develop over a period of several days.

https://doi.org/10.1017/S0022112002008133 Published online by Cambridge University Press

The spanwise patterns were then visible when the growth was illuminated by the scanning laser beam. The entire image of figure 5 was acquired at the same instant. It was partitioned into five sub-images, in order to allow individual image processing, which accounted for variations of illumination intensity with depth. At the instant of acquisition of the image of figure 5, the centreline of the cylinder is midway between the crest and trough of the wave.

Figure 5 shows small-scale white dots distributed in a staggered fashion along the axis of the cylinder at a relatively low value of $KC = 4.5$. These small-scale concentrations are similar to those observed by Honji (1981) at $KC \approx 1$ to 3. This type of instability was subsequently addressed by Sarpkaya (1986), Tatsuno & Bearman (1990), Dütsch *et al.* (1998*b*), Dütsch (2000) and Elston *et al.* (2000), as described in §1. In all of these investigations, the instability was characterized for unidirectional oscillation of a cylinder in quiescent fluid, and the spanwise wavelength λ/D was found to be a function of both KC and β.

In the plot of figure 5 the wavelength λ/D is defined as the spanwise spacing between white dots along the same side of the cylinder; the corresponding image was acquired at 200 cycles after the onset of wave motion. As indicated, the value of λ/D is approximately unity near the lower end of the cylinder where the flow is essentially unidirectional. As the free surface is approached, λ/D increases to a value as high as 4.5, while the axis ratio of the orbital trajectory of the incident wave, i.e. B/A (defined in figure 2) increases as well. Data points corresponding to the experimental values of λ/D versus B/A are also plotted in figure 5, and good correlation is obtained with the variation of λ/D versus z. In addition, the plot of figure 5 shows data points that represent values of λ/D vs. z determined from quantitative PIV images. This technique is described in the next section.

The increase of λ/D near the free surface is expected to be influenced by the boundary condition imposed by the surface. In this regard, its effect may be analogous to that of an end plate in a shear flow, which can stabilize spanwise cells of the flow structure (Stansby 1976). Of course, the free surface forms a boundary that is distinctly different from an end plate; in the ideal limit, the free surface is stress free. Nevertheless, its presence is expected to modify the structure of the spanwise cells.

4.2. *Quantitative images*

Quantitative imaging in the form of high-image-density particle image velocimetry using the digital system described in §2 provided fields of instantaneous velocity vectors $\boldsymbol{V}$, contours of constant horizontal (crossflow) velocity v and modes of instantaneous streamwise vorticity ω_x, as shown in figures 6 and 7. Figure 6(*a*)–6(*c*) were acquired over the field of view indicated in the schematic adjacent to each set of images. In essence, it extended from the free surface to a distance of $10.1D$ beneath the quiescent surface. For the images shown in figures 7(*a*) and 7(*b*), the field of view extended over a distance of $10.1D$ to $20.8D$ beneath the quiescent free surface. For each field of view, two instants during the wave cycle are considered. The first instant is when the centreline of the cylinder is coincident with the trough of the wave, which corresponds to the deepest point on the particle trajectory of the wave. At the second instant, the centreline of the cylinder is midway between the wave trough and crest, which represents the vertical midpoint of the particle trajectory. The instant of image acquisition is designated by the dot on the schematic of the wave particle trajectory, which is shown in each image layout.

In figure 6(*a*), the field of instantaneous velocity vectors $\boldsymbol{V}$ is biased in the downward direction, due to the fact that the axis of the cylinder is located midway between a wave

https://doi.org/10.1017/S0022112002008133 Published online by Cambridge University Press

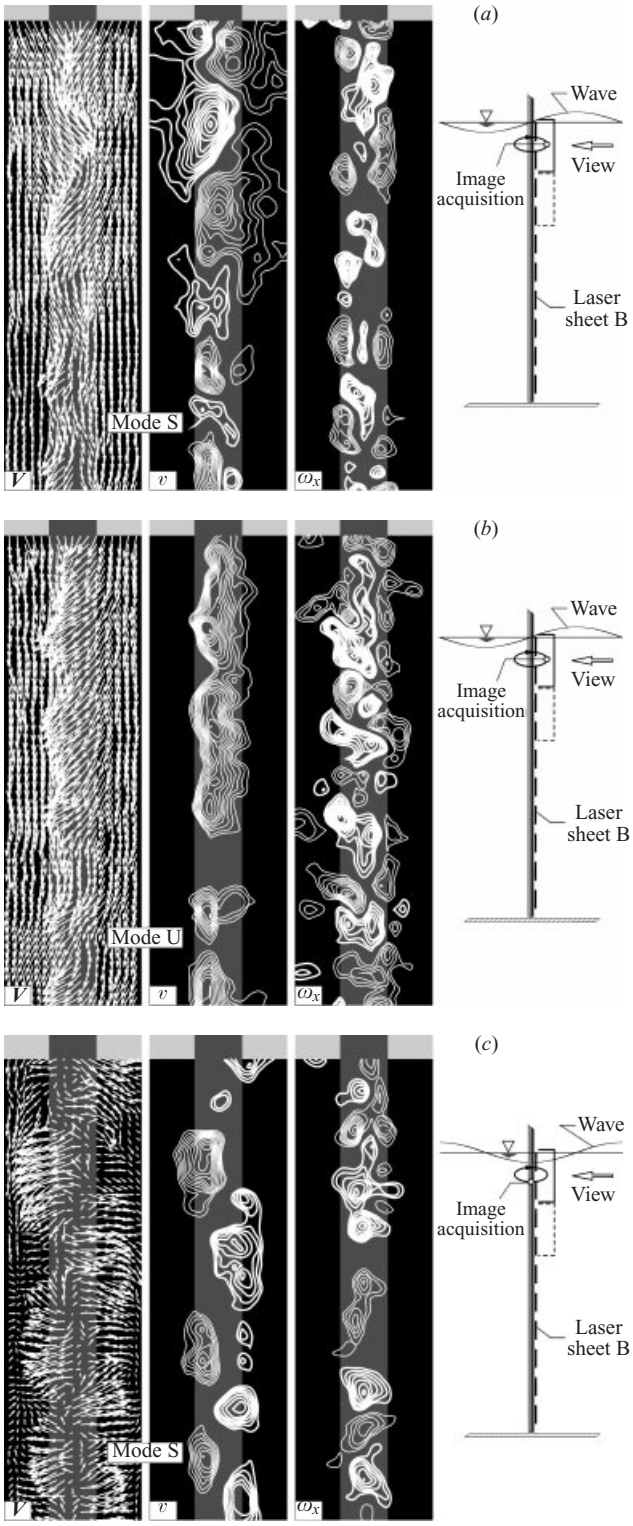


FIGURE 6. For caption see facing page.

https://doi.org/10.1017/S0022112002008133 Published online by Cambridge University Press

trough and crest. The contours of constant horizontal (crossflow) velocity v exhibit a staggered arrangement. The sinuous form of $\boldsymbol{V}$ and the multiple zero crossings of v along the centreline of the cylinder define the basic sinuous mode S, which occurs in somewhat different forms in subsequent sets of images. The corresponding contours of streamwise vorticity ω_x generally show, at a given depth beneath the free surface, pairs of vorticity concentrations of like sign.

The mode S shown in figure 6(a) was, however, not repetitive from cycle to cycle. An alternative mode, represented by the image of figure 6(b), could occur at the same phase of the wave motion. As shown in the images of instantaneous velocity vector $\boldsymbol{V}$ and constant horizontal velocity v, the horizontal components of velocity are all oriented in the same direction, i.e. to the left. That is, the horizontal movement of the near wake is unidirectional. As a result, the contours of v no longer exhibit a staggered arrangement as in figure 6(a); rather they take the form of an in-line arrangement of like sign along the entire span of the cylinder. These arrangements define the unidirectional mode U. The corresponding pattern of vorticity concentration ω_x generally shows alternating positive and negative concentrations along the span of the cylinder.

Figure 6(c) corresponds to the instant at which the trough of the wave is coincident with the centreline of the cylinder. The instantaneous velocity vectors $\boldsymbol{V}$ show an alternating pattern with increasing depth beneath the free surface. Contours of constant horizontal velocity v show a corresponding staggered pattern, which is analogous to that shown in figure 6(a). This pattern thereby satisfies the criterion of the sinuous mode S of figure 6(a). The wavelength λ of the pattern of v in figure 6(c) is relatively large near the free surface and decreases with depth, again in accord with the variation of figure 6(a). At a depth sufficiently far beneath the free surface, the staggered arrangement of v contours corresponds to an aligned arrangement of streamwise vorticity ω_x, which is centred on the image of the cylinder. Values of dimensionless wavelength λ/D as a function of depth z obtained from figure 6(c) are indicated by the solid black symbols in the plot of figure 5.

Images at a larger depth beneath the free surface are shown in figures 7(a) and 7(b). They exhibit a more ordered, repetitive form, relative to those near the free surface. At the phase of the wave motion shown in figure 7(a), which corresponds to the cylinder position midway between a trough and a crest, the overall form of the instantaneous velocity field $\boldsymbol{V}$ shows a sinuous form, and the contours of horizontal velocity v show a staggered arrangement, thereby representing the sinuous mode S. The corresponding arrangement of vorticity concentration ω_x tends to show a pair of like sign at each depth.

Figure 7(b) represents the case where the trough of the wave is coincident with the centreline of the cylinder. The form of $\boldsymbol{V}$ indicates local jet-like flows directed

FIGURE 6. Representations of the sinuous mode S and unidirectional mode U over a field of view immediately beneath the free surface, where $KC = 4.5$. KC decreases with depth and at the bottom edge of the images $KC = 4.0$. The left-hand images show the field of instantaneous velocity vectors $\boldsymbol{V}$, the middle images show contours of constant positive (thick line) and negative (thin line) horizontal velocity v, and the right-hand images show corresponding modes of the instantaneous streamwise vorticity ω_x. In (a, b) at the instant of image acquisition the centreline of the cylinder is located midway between the trough and crest of the wave; in (c) it coincides with the trough. (a) Sinuous mode S: the minimum of v, $v_{min} = 2\,\mathrm{mm\,s^{-1}}$ and incremental Δv values are $1\,\mathrm{mm\,s^{-1}}$; for the vorticity plots the minimum $(\omega_x)_{min} = 0.6\,\mathrm{s^{-1}}$ and incremental $\Delta\omega_x$ values are $0.2\,\mathrm{s^{-1}}$. (b) Unidirectional mode U: $v_{min} = 4\,\mathrm{mm\,s^{-1}}$, $\Delta v = 1\,\mathrm{mm\,s^{-1}}$, $(\omega_x)_{min} = 0.4\,\mathrm{s^{-1}}$, $\Delta\omega_x = 0.2\,\mathrm{s^{-1}}$. ($c$) Sinuous mode S: $v_{min} = 3\,\mathrm{mm\,s^{-1}}$, $\Delta v = 0.5\,\mathrm{mm\,s^{-1}}$ $(\omega_x)_{min} = 0.4\,\mathrm{s^{-1}}$, $\Delta\omega_x = 0.2\,\mathrm{s^{-1}}$.

https://doi.org/10.1017/S0022112002008133 Published online by Cambridge University Press

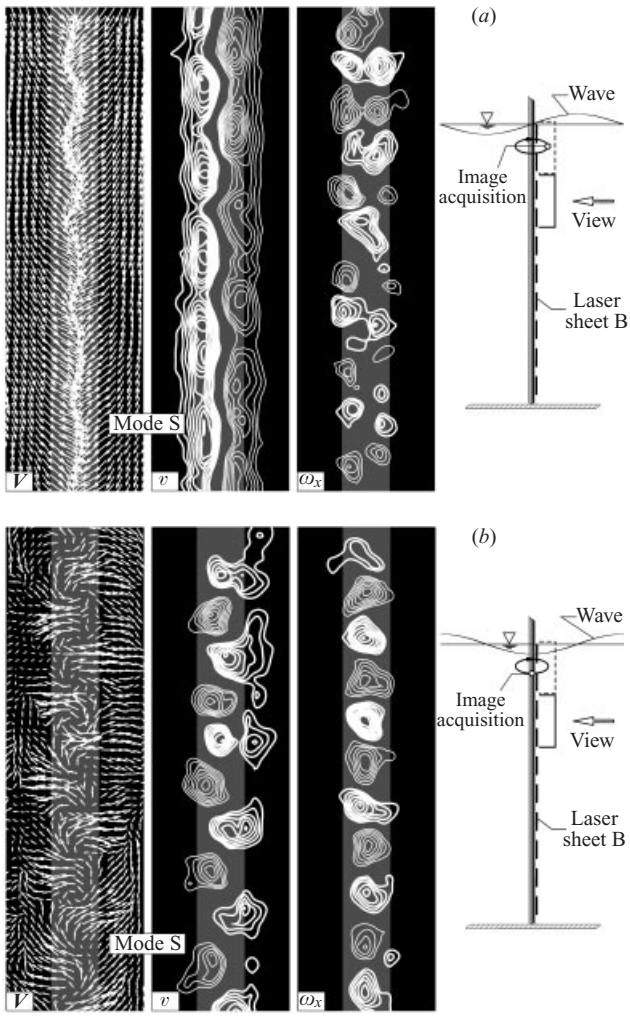


FIGURE 7. As figure 6 but showing sinuous mode S for a lower field of view: each image is over a distance of $10.0D$ to $20.8D$ beneath the elevation of the quiescent free surface. $KC = 4.0$ and 3.6 at the top and bottom edges of each image respectively. In (a) at the instant of image acquisition the centreline of the cylinder is located midway between the trough and crest of the wave; in (b) it coincides with the trough. (a) $v_{min} = 4\,\mathrm{mm\,s^{-1}}$, $\Delta v = 1\,\mathrm{mm\,s^{-1}}$, $(\omega_x)_{min} = 0.4\,\mathrm{s^{-1}}$, $\Delta\omega_x = 0.2\,\mathrm{s^{-1}}$. ($b$) $v_{min} = 2\,\mathrm{mm\,s^{-1}}$, $\Delta v = 0.5\,\mathrm{mm\,s^{-1}}$, $(\omega_x)_{min} = 0.4\,\mathrm{s^{-1}}$, $\Delta\omega_x = 0.2\,\mathrm{s^{-1}}$.

away from the centreline of the cylinder, and contours of constant horizontal velocity v show the staggered form of the sinuous mode S. Again, the values of wavelength between these contours are indicated by the black dots on the plot of figure 5. The corresponding modes of vorticity ω_x are remarkably well aligned with the centreline of the cylinder.

Taken together, the images of figures 6 and 7 suggest that near the free surface, where the wave particle orbits have a significant value of ellipticity B/A, the modes of horizontal velocity v and streamwise vorticity ω_x are less repetitive and organized, relative to those further beneath the free surface where B/A becomes smaller. This enhanced organization with increasing depth beneath the free surface may also be

https://doi.org/10.1017/S0022112002008133 Published online by Cambridge University Press

aided by the decrease of KC, which is, however, considerably milder than the decrease of B/A.

Values of dimensionless circulation $\Gamma^* = \Gamma/UDKC$ were determined for representative, isolated concentrations of streamwise vorticity ω_x in figures 6 and 7. In the region immediately beneath the free surface, represented by figure 6, the vorticity concentrations have a relatively large scale, and $|\Gamma^*| = 0.13$ to 0.16. Further beneath the free surface, the concentrations are smaller and their arrangement is highly ordered, at least at the proper phase of the wave cycle. The values of dimensionless circulation are $|\Gamma^*| = 0.06$ to 0.09. As discussed in conjunction with figure 4, the locally two-dimensional, small-scale vortices have values of circulation, based on patterns of ω_z, of $|\Gamma^*| = 0.12$ to 0.16. It is therefore evident that the strength of the three-dimensional mode based on patterns of ω_x is of the same order as that of the locally two-dimensional mode based on ω_z.

5. Moderate- and large-scale spanwise modes

The previous section focused on low Keulegan–Carpenter number, for which locally two-dimensional, small-scale vortices remain in the immediate proximity of the cylinder. The spanwise modes have values of dimensionless wavelength in the range $1 \leqslant \lambda/D \leqslant 4.5$. At higher values of KC, e.g. 10 and 18, locally two-dimensional, large-scale vortices are shed, and they move well away from the cylinder, as indicated by the shadowgraph visualization of figure 3, and the velocity images of figure 4. Spanwise modes can have values of λ/D that are one to two orders of magnitude larger than those at low KC, as addressed in the following.

5.1. *Qualitative visualization*

Figure 8 shows images of the three-dimensionality for a larger value of $KC = 10$. They were obtained using the same type of illumination of microbial growth as for figure 5. Each image was acquired at a specified number of cycles N after onset of the wavemaker. All images were, however, acquired at the same instant, or phase, of the wave motion. The centreline of the cylinder was midway between the trough and crest of the wave, corresponding to the mid-depth of the vertical portion of the trajectory of the particle wave motion. (See schematic in the inset of figure 6*a*).

The image corresponding to $N = 2$ indicates barely discernible spanwise distortion; at this low value of N, corresponding to a short time after onset of the wavemaker, the wave has not yet attained its steady-state form. At a substantially longer time after the start-up, corresponding to $N = 8$, the spanwise pattern takes on a sinuous form, which is designated as mode S. This mode S degenerates to a simplified form at $N = 170$; it exhibits a single zero crossing, as opposed to the multiple zero crossings of mode S at $N = 8$. Finally, a limiting form of the spanwise structure corresponds to a unidirectional mode U, which is attained at $N = 250$. This qualitative visualization provides a basis for quantitative characterization of the near wake structure, which is described in the next section.

5.2. *Quantitative images*

5.2.1. *Basic spanwise modes*

The spanwise modes of three-dimensional flow structure, which are qualitatively identified in figure 8, are characterized quantitatively in figures 9–11. For all images, the laser sheet orientation B, defined in figures 1(*a*) and 1(*b*), is employed in conjunction with the mirror–camera systems (3) and (4), illustrated in figure 1(*a*). These

https://doi.org/10.1017/S0022112002008133 Published online by Cambridge University Press

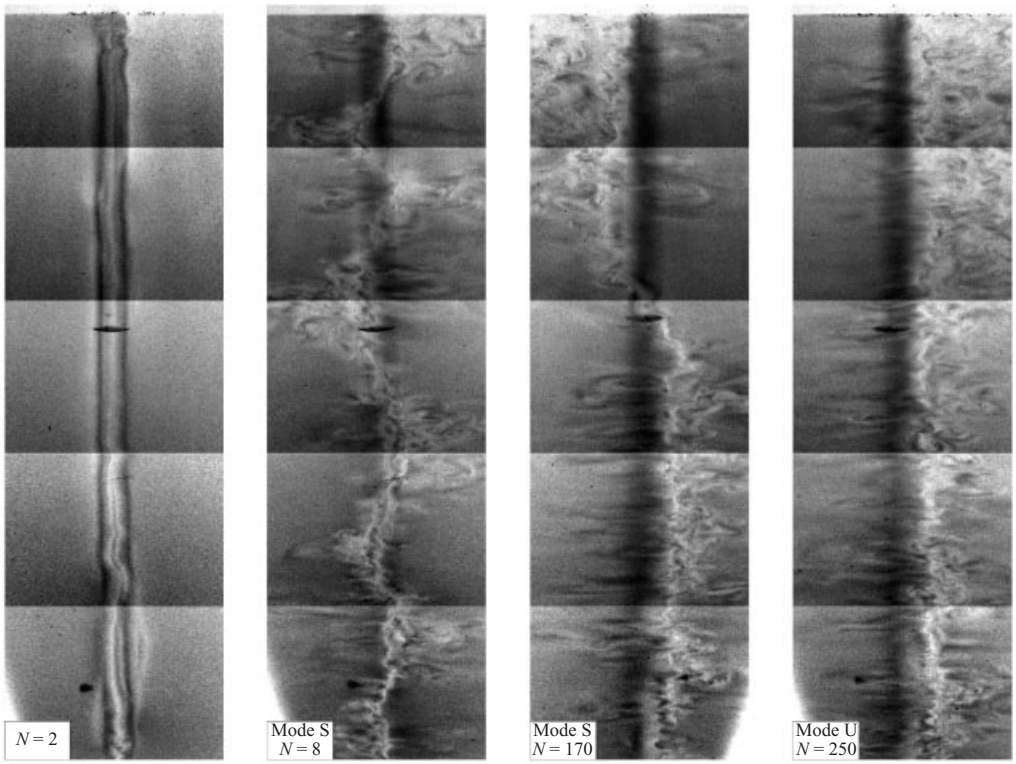


FIGURE 8. Images of spanwise modes which represent the variation of the locally two-dimensional mode of vortex formation along the cylinder; $KC = 10$ at the free surface. N represents the number of cycles of wave motion that have elapsed prior to acquisition of each image. Images are produced by illumination of microbial suspensions in water, using the same approach as for figure 5.

instantaneous features of the flow structure are compared with the instantaneous values of the moment coefficients C_x^* and C_y^* due to in-line and transverse forces respectively.

The image at the left of figure 9(a) shows a quasi-sinusoidal form of the velocity vector field $\boldsymbol{V}$ along the span of the cylinder. The corresponding contours of constant horizontal velocity v show multiple zero crossings along the centreline of the cylinder image, which corresponds to a long-wavelength version of the sinuous mode S described in § 5.1. In essence, the positive and negative regions of v correspond respectively to mode I and mode II of the locally two-dimensional vortex formation shown in figure 4 for $KC = 10$.

Mode S is defined to occur when there is one or more zero crossings of the distribution of horizontal velocity component along the span of the cylinder; this definition is consistent with that employed for low KC in § 4.2. The distance between zero crossings, and thereby the effective wavelength, is substantially larger than the cases addressed at lower KC in § 4. It is relatively large near the free surface and decreases as the bottom of the wave tank is approached. Near the free surface, the distance between zero crossings is approximately $10D$, but near the lower end of the cylinder, where the oscillatory flow is essentially unidirectional, the distance can be as small as $5D$. The local wavelength λ may be taken as twice the local distance between zero crossings, so near the free surface, $\lambda/D \approx 20$ and at the lower end of the cylinder, $\lambda/D \approx 10$. The spanwise wavelength (λ/D) of this quasi-sinusoidal mode S decreases

https://doi.org/10.1017/S0022112002008133 Published online by Cambridge University Press

with increasing depth z beneath the free surface, and therefore with decreasing ratio of the minor to major axes of the particle orbit of the wave, i.e. B/A, as shown in figure 5. The magnitude of the moment coefficient C_y^* due to the transverse force is barely discernable, as evident from the time trace at the bottom of figure 9(a).

The sinuous mode S indicated in the left-hand set of images can degenerate to the form shown in the middle set of images of figure 9(a). In this case, the contours of horizontal velocity v indicate that v is oriented to the right along the upper and lower portions of the cylinder, which corresponds to the occurrence of mode I of the locally two-dimensional vortex shedding (compare figure 4, $KC = 10$). On the other hand, near the centre of the cylinder, v is to the left, which corresponds to mode II. Again, this particular form of mode S corresponds to a very small value of C_y^*, as indicated in the corresponding moment trace.

Finally, the case of a single zero crossing of the horizontal velocity is shown in the right-hand set of images of figure 9(a). This pattern indicates that modes I and II of the locally two-dimensional vortex formation (compare figure 4) occur respectively along the lower and upper regions of the cylinder. This form of mode S is associated with detectable magnitudes of C_y^*, as evident in the moment trace. This is due to larger contributions to the moment acting on the cylinder for larger depths, where there is unidirectional shedding over a significant fraction of the span.

Obasaju *et al.* (1988) reported, on the basis of qualitative observation, a two-cell structure along the span of the cylinder, whereby each cell occupied about half of the span. This two-cell mode appears to be the same as the mode shown in the right set of images of figure 9(a).

As shown in figure 9(b), similar modes can occur at a higher value of $KC = 18$. For all sets of images, positive and negative contours of horizontal velocity v correspond respectively to modes I and II of locally two-dimensional vortex formation (compare figure 4, $KC = 18$). Generally speaking, at this larger value of wave amplitude, the modes are not as sharply defined as those of figure 9(a) corresponding to $KC = 10$. This observation is particularly true for the region near the free surface where the vertical component of velocity associated with the orbital trajectory of the wave is relatively large. Furthermore, as shown in the left set of images, the quasi-sinusoidal variation of transverse velocity along the span of the cylinder, which is characteristic of mode S, is not as regular as at the lower value of $KC = 10$ exhibited in figure 9(a). Degenerate forms of mode S are shown in the middle and right-hand set of images. The mode S with a single zero crossing, which is shown in the right-hand set of images of figure 9(b), produces detectable peaks of the C_y^* trace, relative to the very low magnitudes associated with forms of mode S that have a larger number of zero crossings. This observation is the same as for $KC = 10$ in figure 9(a).

An interesting issue is the possibility of a unidirectional spanwise mode U, which corresponds to the same sign of the transverse velocity v along the entire span of the cylinder. As indicated in figure 10, it is indeed possible to attain such a mode for both $KC = 10$ and 18. The region near the free surface at the higher value of $KC = 18$ exhibits a more complex form due to the relatively large amplitude of the wave motion. These unidirectional U modes can be sustained for a relatively large number of wave cycles, as addressed below. They are therefore quite robust and their existence is not precluded by variations of the ellipticity ratio B/A of the wave particle trajectory and KC along the span of the cylinder. The traces of the moment coefficient C_y^* due to the transverse force for these unidirectional modes U exhibit, of course, relatively large magnitudes in comparison with the magnitudes for the sinuous S modes.

https://doi.org/10.1017/S0022112002008133 Published online by Cambridge University Press

(*a*)

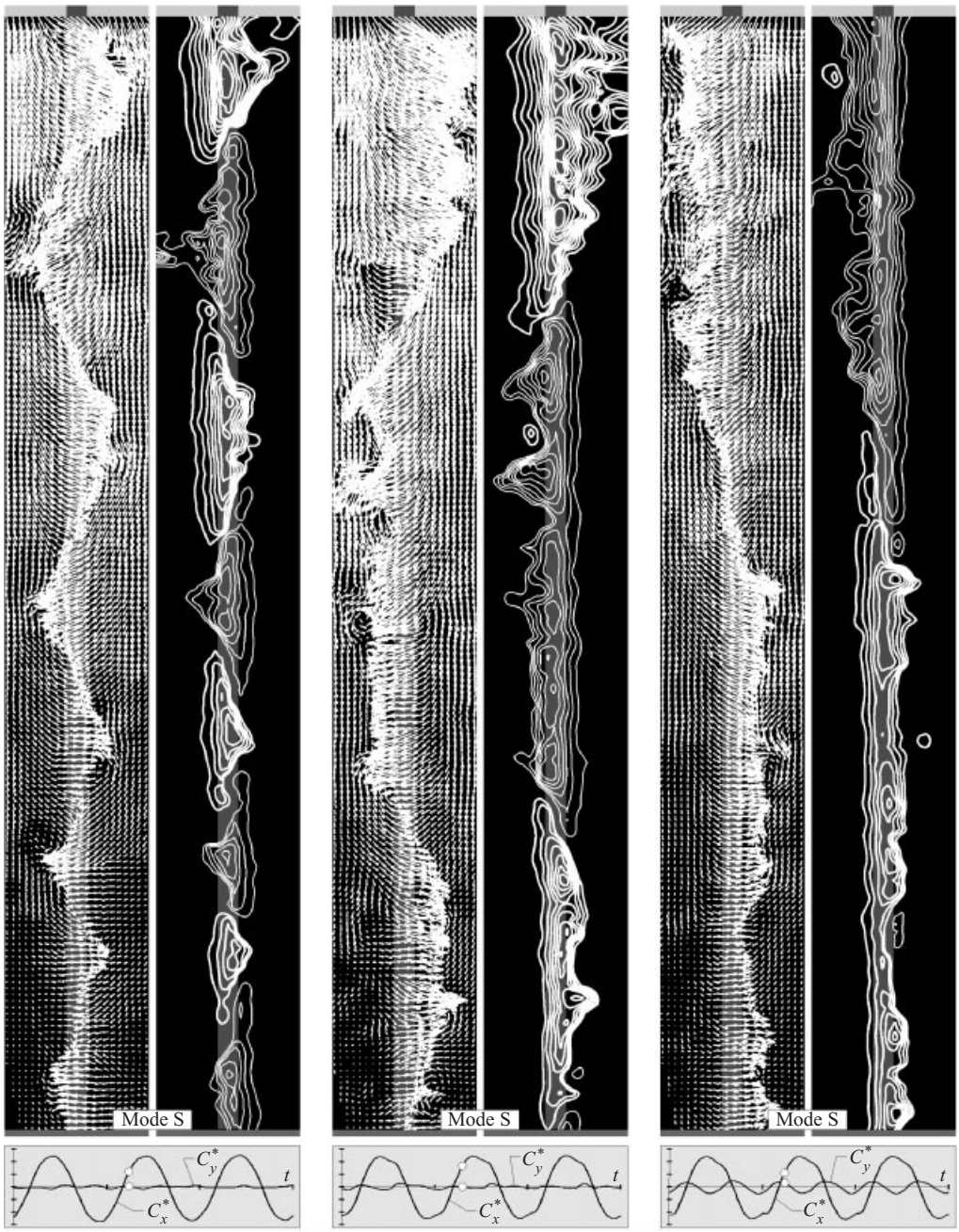


FIGURE 9. For caption see facing page.

5.2.2. *Spanwise modes in terms of streamwise vorticity*

Further insight into the spanwise modes S and U described in the foregoing is provided by the vorticity contours shown in figure 11. Representative distributions of instantaneous velocity $\boldsymbol{V}$, taken from figures 9 and 10, are directly compared with contours of constant positive (thick white line) and negative (thin white line)

https://doi.org/10.1017/S0022112002008133 Published online by Cambridge University Press

(*b*)

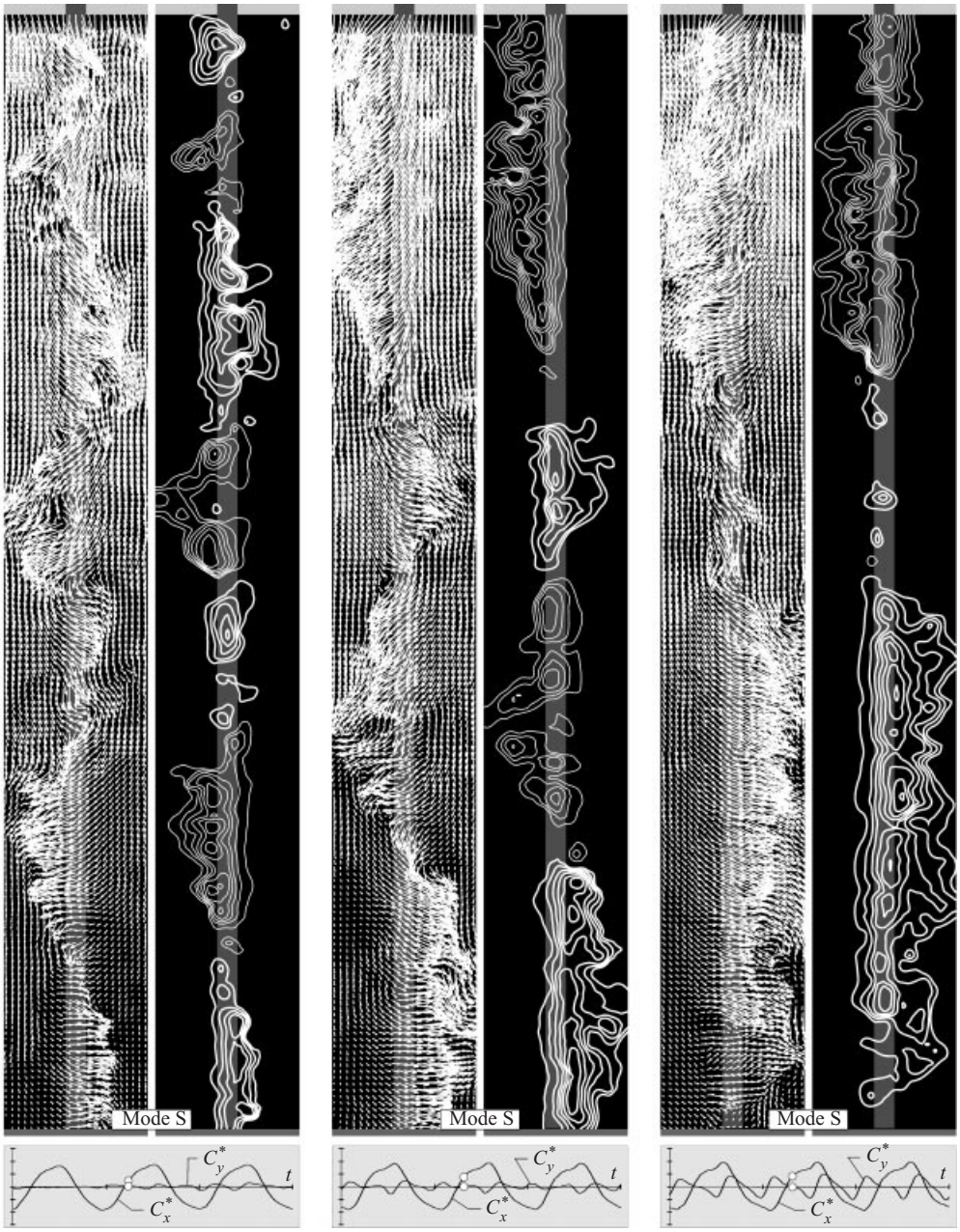


FIGURE 9. (*a*, *b*) Images of sinuous modes S that represent the variation of the locally two-dimensional mode of vortex formation (compare figure 4) along the span of the cylinder. Instantaneous modes of velocity vectors $\boldsymbol{V}$ are compared with contours of constant horizontal velocity v; (*a*) $KC = 10$ at the free surface; $v_{min} = 10\,\mathrm{mm\,s^{-1}}$, $\Delta v = 5\,\mathrm{mm\,s^{-1}}$; (*b*) $KC = 18$ at the free surface; $v_{min} = 20\,\mathrm{mm\,s^{-1}}$, $\Delta v = 10\,\mathrm{mm\,s^{-1}}$.

https://doi.org/10.1017/S0022112002008133 Published online by Cambridge University Press

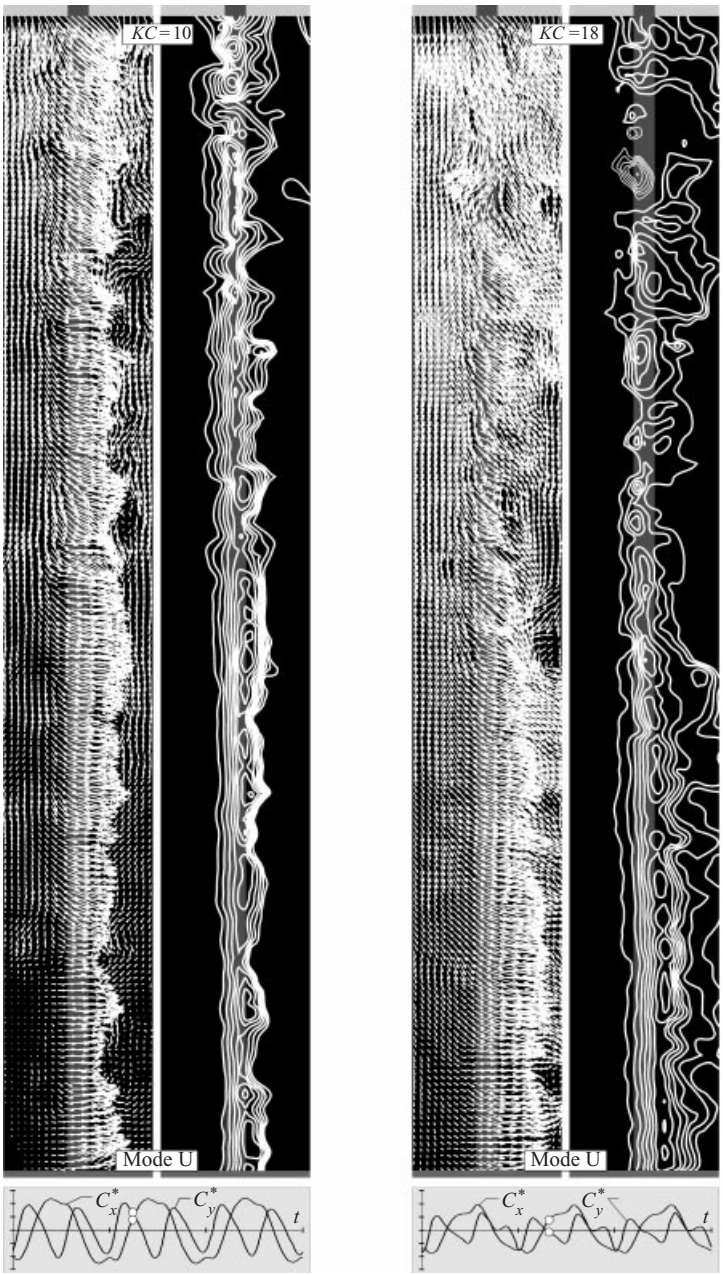


FIGURE 10. Representations of the unidirectional mode U. Modes of instantaneous velocity vectors $\boldsymbol{V}$ and contours of constant horizontal velocity v correspond to a consistent locally two-dimensional mode of vortex formation (compare figure 4) along the span of the cylinder for $KC = 10$, $v_{min} = 10\,\mathrm{mm\,s^{-1}}$, $\Delta v = 5\,\mathrm{mm\,s^{-1}}$ (left-hand set of images) and $KC = 18$, $v_{min} = 20\,\mathrm{mm\,s^{-1}}$, $\Delta v = 10\,\mathrm{mm\,s^{-1}}$ (right-hand set of images).

streamwise vorticity ω_x. Consider, first, mode S at $KC = 10$. The overall form of the arrangement of vorticity concentrations along the span of the cylinder closely follows the form of the instantaneous velocity vector field $\boldsymbol{V}$. These concentrations of streamwise vorticity ω_x must be located in the vorticity layer originally shed from the

https://doi.org/10.1017/S0022112002008133 Published online by Cambridge University Press

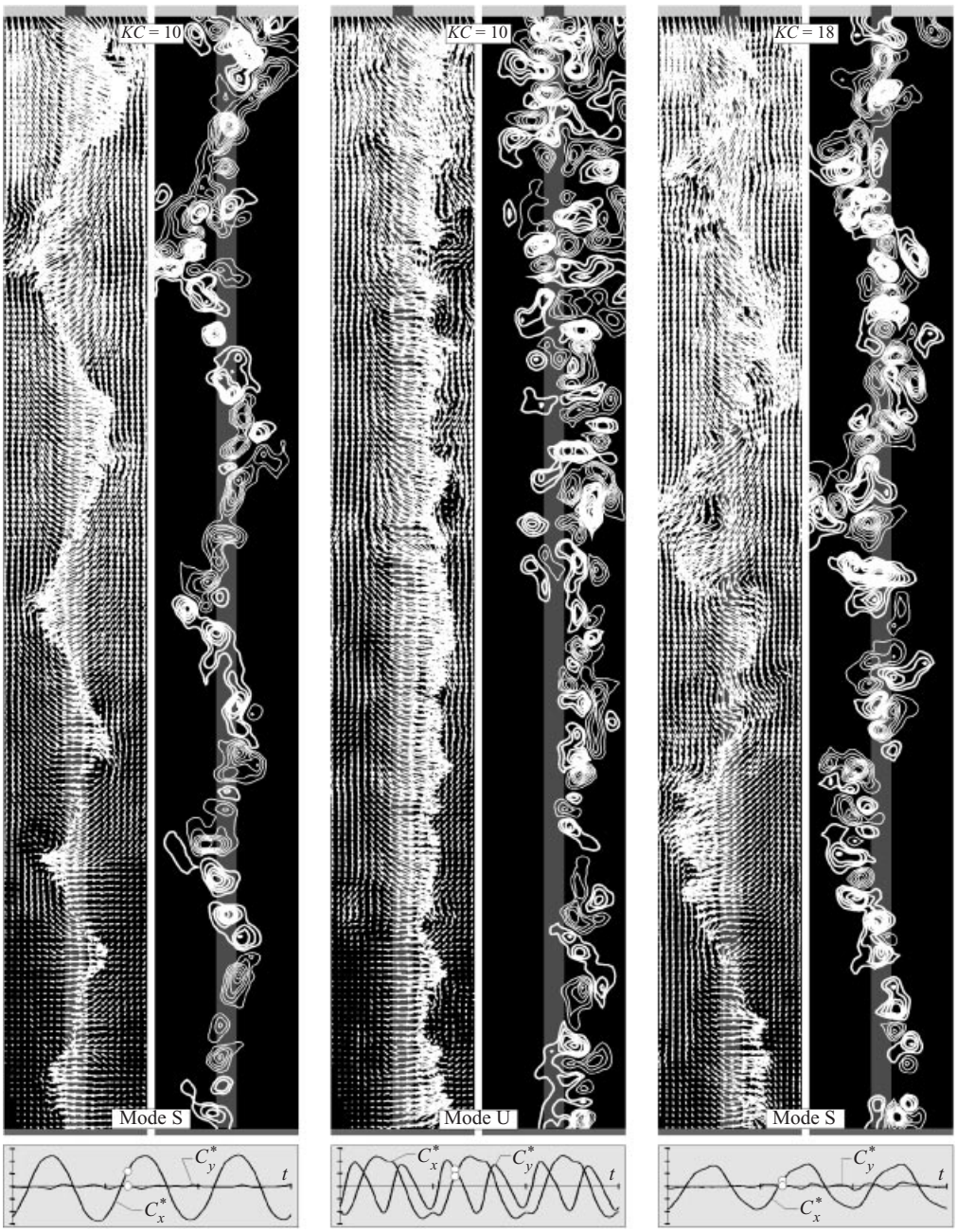


FIGURE 11. Modes of instantaneous velocity vectors $\boldsymbol{V}$ and contours of constant streamwise vorticity ω_x for representative spanwise modes shown in figures 9 and 10. $KC = 10$: $(\omega_x)_{min} = 0.5\,\mathrm{s}^{-1}$, $\Delta\omega_x = 0.5\,\mathrm{s}^{-1}$; $KC = 18$: $(\omega_x)_{min} = 1\,\mathrm{s}^{-1}$, $\Delta\omega_x = 1\,\mathrm{s}^{-1}$.

surface of the cylinder. The large-scale, spanwise distortion of the ω_x arrangement is therefore compatible with the change of the mode of locally two-dimensional vortex shedding (compare figure 4) along the span of the cylinder.

Regarding the individual vorticity concentrations in the mode S at $KC = 10$, the spacing between them is in the range $1.5D$ to $4D$, in contrast to the long

https://doi.org/10.1017/S0022112002008133 Published online by Cambridge University Press

wavelengths $10 \leqslant \lambda/D \leqslant 20$ of the large-scale spanwise distortion. In the region near the free surface, corresponding to roughly the uppermost one-fourth of the cylinder, the arrangement of the vorticity concentrations becomes more complex, due to the substantial vertical component of velocity in that region.

The arrangement of vorticity concentrations of mode U at $KC = 10$, which is shown in the middle set of images of figure 11, does not show large-scale distortion. That is, the sinusoidal, large-scale undulations of the mode S are not present. This observation is in accord with the quasi-unidirectional distribution of the instantaneous velocity. Over the lower portion of the cylinder, where a representative spanwise spacing between vorticity concentrations can be defined, it has values in the range $1D$ to $4D$. Along the upper portion of the cylinder, where the axis ratio of the particle trajectory of the wave is relatively large, the pattern of vorticity concentrations becomes more complex.

Finally, the case of mode S at $KC = 18$ is shown in the right-hand set of images of figure 11. It shows a large-scale sinusoidal distortion of the vorticity pattern, which again is in accord with the overall form of the instantaneous velocity field $\boldsymbol{V}$. The spacing between the small-scale vorticity concentrations is approximately $1D$ to $4D$ along the entire span.

Taken together, the three sets of images of figure 11 suggest that variation of the mode of locally two-dimensional vortex shedding (compare figure 4) along the span of the cylinder is indicated by large-scale spanwise modes of both instantaneous velocity and vorticity, and they provide complementary descriptions. These large-scale distortions are not associated with corresponding large-scale concentrations of streamwise vorticity. Only small-scale concentrations of vorticity are detectable. They lack spatial periodicity, but it is possible to discern approximate values of spacing between them of $1D$ to $4.5D$. Evaluation of the dimensionless circulation Γ^*, based on the concentrations of streamwise vorticity ω_x, gives values in the range $0.10 \leqslant |\Gamma^*| \leqslant 0.17$. These values compare with $0.06 \leqslant |\Gamma^*| \leqslant 0.16$ observed at low KC.

5.2.3. *Transverse loading in relation to spanwise modes*

In figures 9–11, direct comparisons were made with the instantaneous values of moment coefficients C_y^* and C_x^* due to transverse and in-line forces at a given instant of time. The magnitude of C_y^* is generally a strong function of the degree of uniformity of the instantaneous spanwise mode. An attempt was made to estimate the instantaneous amplitude of the moment coefficient due to the transverse force based on the degree of unidirectionality of the instantaneous contours of constant horizontal velocity along the span of the cylinder. This estimate was performed for the case $KC = 10$, where the spanwise modes are sharply defined. The procedure is as follows. The schematic of figure 12 shows contours of constant negative (thin line) and positive (thick line) horizontal velocity. The distance between zero crossings of positive and negative contours is designated as $\ell_1, \ell_2 \ldots \ell_n$, and distances from the centroid of each respective set of contours to the centre of the strain gauge system as $L_1, L_2 \ldots L_n$. For the present approximation, the peak amplitude of the measured moment due to the transverse force was used to obtain a transverse force coefficient C_y' by assuming that it acts at the mid-depth of the submerged cylinder. The peak value of the moment occurred immediately prior to acquisition of an image corresponding to mode U. Values of the moment coefficient C_y^* due to the transverse force were

https://doi.org/10.1017/S0022112002008133 Published online by Cambridge University Press

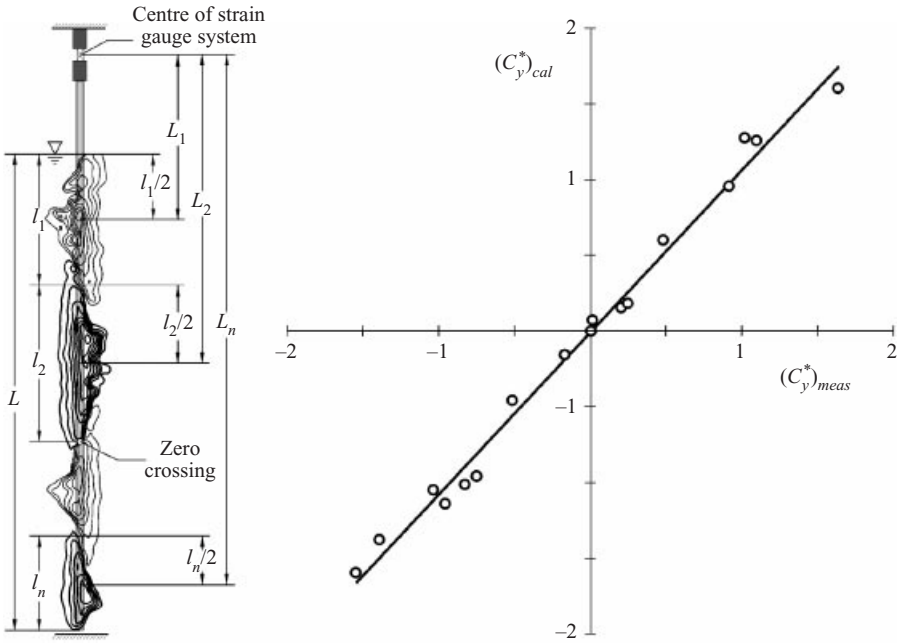


FIGURE 12. Plot of the moment coefficient $(C_y^*)_{cal}$ due to the transverse force versus measured value $(C_y^*)_{meas}$. $KC = 10$. $(C_y^*)_{cal}$ was calculated using a simple weighting formula based on the mode that represents the variation of the locally two-dimensional mode of vortex formation along the cylinder at a given instant. Straight line represents $(C_y^*)_{cal} = (C_y^*)_{meas}$.

calculated according to

$$(C_y^*)_{cal} = \frac{(\ell_1 L_1 + \ell_2 L_2 + \cdots + \ell_n L_n)(C_y')}{(\ell_1 + \ell_2 + \cdots + \ell_n)L}.$$

It should be noted that the signs in front of each of the products $\ell_i L_i$, where $i = 1, 2, \ldots$, are determined by the local direction of the horizontal component of velocity, which represents the occurrence of either mode I or mode II (see figure 4). Values of $(C_y^*)_{cal}$ versus $(C_y^*)_{meas}$ are shown in figure 12, where $(C_y^*)_{meas}$ is the measured peak value of the moment coefficient due to the transverse force immediately prior to acquisition of the PIV image. Each data point $(C_y^*)_{meas}$ in figure 12 corresponds to a different PIV image and, generally speaking, to a somewhat different arrangement of contours of constant horizontal velocity. Remarkably, this crude estimate provides a reasonable indication of the magnitude of the instantaneous moment coefficient due to the transverse force based strictly on imaging of the spanwise structure. Of course, it does not account for possible distortions of the basic mode of quasi-two-dimensional vortex shedding along the span of the cylinder, or the individual values of circulation of each vortex within these modes.

5.2.4. *In-line loading in relation to spanwise modes*

The time traces of the moment coefficient C_x^* due to the in-line force shown in figures 9–11 appear to be relatively unaffected by the spanwise mode of three-dimensionality. Phase-referenced time traces of C_x^* are superposed in figure 13. They were triggered with respect to the wave motion. The small hollow circular symbols indicate the instant at which the image was acquired for each moment trace. At

https://doi.org/10.1017/S0022112002008133 Published online by Cambridge University Press

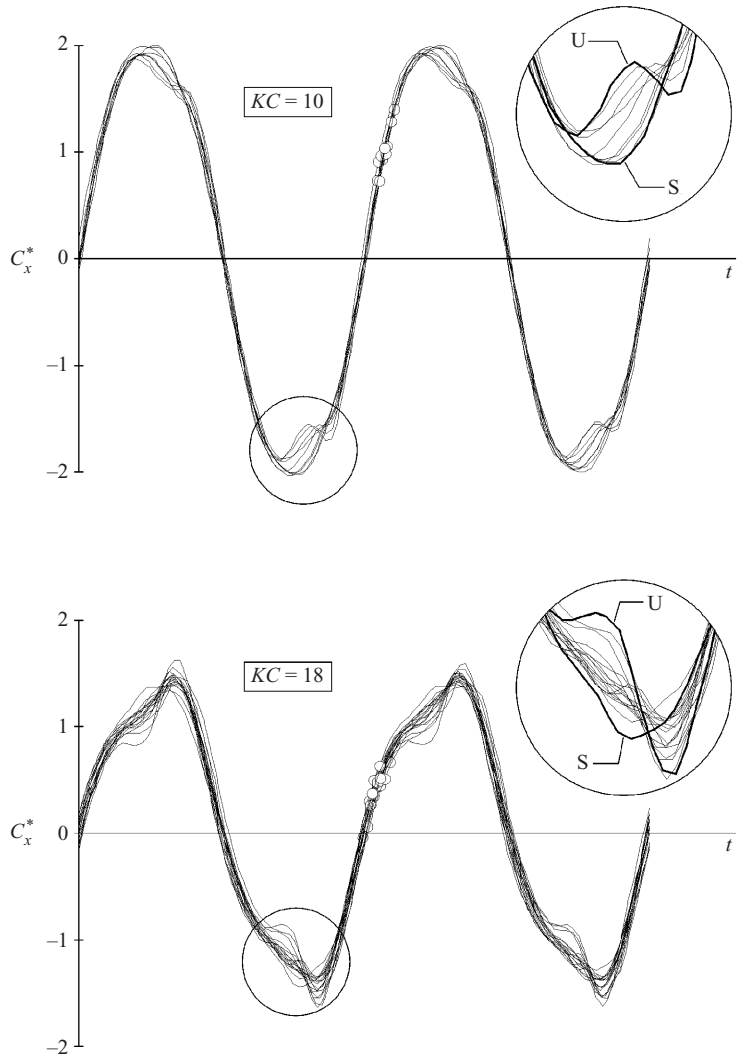


FIGURE 13. Variations of the moment coefficient C_x^* due to the in-line force with time for different spanwise modes. Symbols S and U correspond respectively to mode S (very low value of moment coefficient C_y^* due to the transverse force) shown in figure 9(*a*, *b*) and mode U (large value of moment coefficient C_y^* due to the transverse force) shown in figure 10.

$KC = 10$ (upper plot) and 18 (lower plot), a total of 10 and 15 traces respectively are superposed. Deviations are most evident at and near the negative and positive peaks. These deviations were compared with the corresponding images. As indicated in the zoomed-in views of figure 13, the extreme values of C_x^* at these peaks are associated with the sinuous mode S that has multiple zero crossings and the quasi-unidirectional mode U defined in figures 8–11.

6. Overview of averaged unsteady loading on the cylinder

In the preceding sections, emphasis is on quantitative representations of the three-dimensional flow modes in the near wake of the cylinder. Short segments of in-

https://doi.org/10.1017/S0022112002008133 Published online by Cambridge University Press

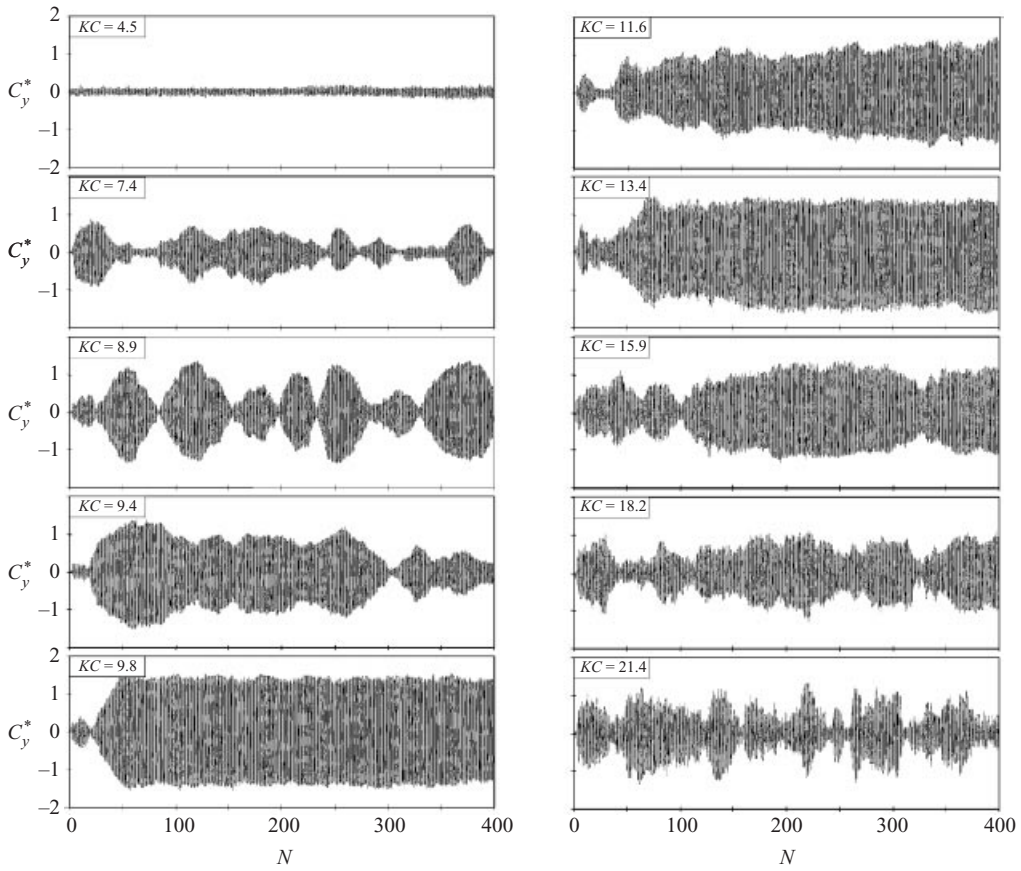


FIGURE 14. Time traces of the moment coefficient C_y^* due to the transverse force for various values of KC. The time axis on each trace is represented by N, which corresponds to the number of cycles after the onset of wave motion.

stantaneous moment traces were illustrated, in order to allow correlation of the instantaneous values of moment coefficients C_x^* and C_y^* due to in-line and transverse forces with the images. In view of the fact that a number of basic modes of three-dimensionality can occur, and spontaneous transitions between modes were observed, it is expected that long-time records of the moment coefficient C_y^* due to the transverse force will exhibit substantial amplitude modulation.

Figure 14 shows traces of C_y^* as a function of N, in which N is the number of cycles from onset of the wavemaker. A maximum of 400 cycles, i.e. $N = 400$, is shown at each value of $KC = 2\pi A_0/D = 2\pi(A/2)/D$. At most values of KC, severe amplitude modulation is evident. The period of this modulation is typically of the order of 30 to 50 cycles, though significantly shorter and longer modulation periods are discernible in certain of the traces. At $KC = 9.8$ to 13.4, it is possible to attain a trace that exhibits relatively minor amplitude modulation, but only after a minimum number of cycles $N = 50$ to 200 has elapsed. It should be noted that the highly persistent trace at $KC = 9.8$ is related to the case at $KC = 10$ for unidirectional oscillatory flow past a stationary cylinder. Obasaju *et al.* (1988) found highly correlated spanwise pressure fluctuations along the span of the cylinder at $KC = 10$. Moreover, Williamson

https://doi.org/10.1017/S0022112002008133 Published online by Cambridge University Press

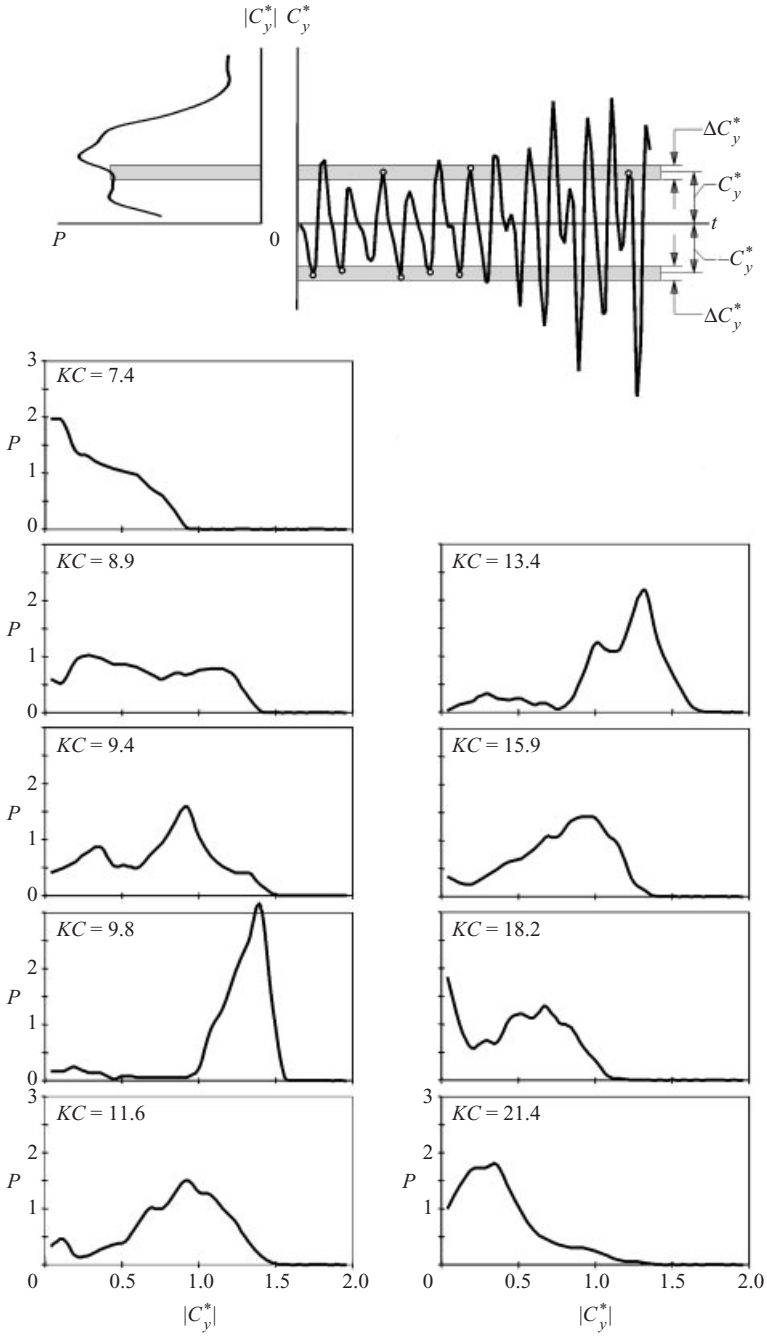


FIGURE 15. Plots of probability density P of the moment coefficient C_y^* due to the transverse force for various values of KC. $P(C_y^*) = (n/N)/\Delta C_y^*$, $\int_0^\infty P(C_y^*)\,\mathrm{d}C_y^* = 1$, where n is the number of peaks in ΔC_y^* and N is the total number of all peaks.

(1985) and Obasaju *et al.* (1988) observed the peak magnitude of the transverse force coefficient C_y to occur at or in the vicinity of $KC = 10$.

The highly modulated traces of the moment coefficient C_y^* due to the transverse force in figure 14 suggest that a proper statistical representation of the loading would

https://doi.org/10.1017/S0022112002008133 Published online by Cambridge University Press

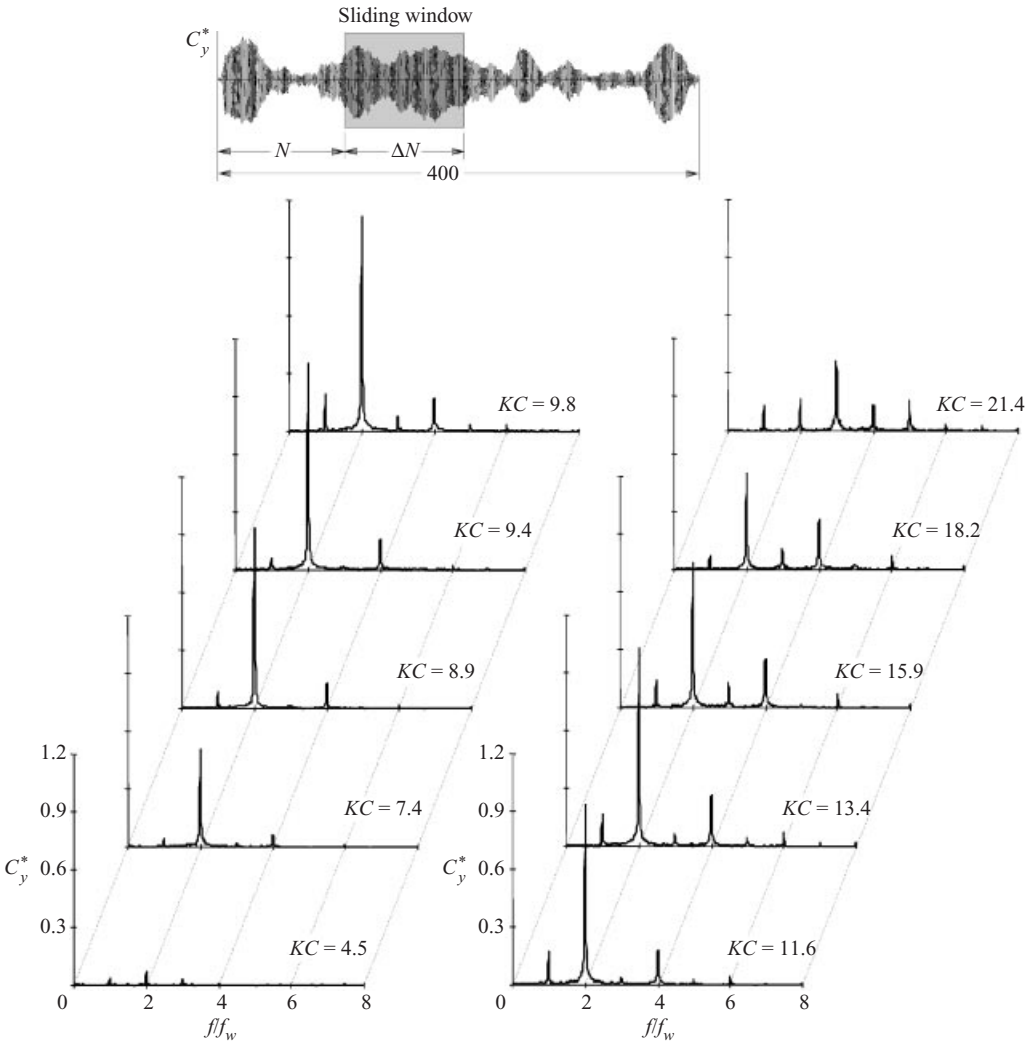


FIGURE 16. Spectra of the moment coefficient C_y^* due to the transverse force as a function of frequency, normalized by the frequency f_w of the wave for the indicated values of KC. All spectra were calculated using a sliding window with $\Delta N = 50$.

be a type of probability density P. The schematic at the top of figure 15 shows the technique employed to evaluate the probability $P(C_y^*)$. Either a positive or negative peak occurs in a window of width ΔC_y^* displaced a distance corresponding to C_y^* from a zero position. The number of peaks within a given window is represented by n. The total number of peaks is N and the probability density is therefore $P(C_y^*) = [n/N]/\Delta C_y^*$. The plots of probability density P exhibited in figure 15 show well-defined peaks at relatively large values of $KC = 9.8$ and 13.4. These peaks occur in the range $1.3 \leqslant |C_y^*| \leqslant 1.4$. For values of KC successively lower than $KC = 9.8$, the peak of P shifts to lower C_y^* at $KC = 9.4$, becomes relatively flat at $KC = 8.9$ and exhibits a peak at very low C_y^* for $KC = 7.4$. A generally similar trend is evident for values of $KC > 13.4$. For $KC = 15.9$, 18.2 and 21.4, the peak is attenuated and moves to successively lower values of C_y^*.

Corresponding spectra for each of the time traces of figure 14 are exhibited in

https://doi.org/10.1017/S0022112002008133 Published online by Cambridge University Press

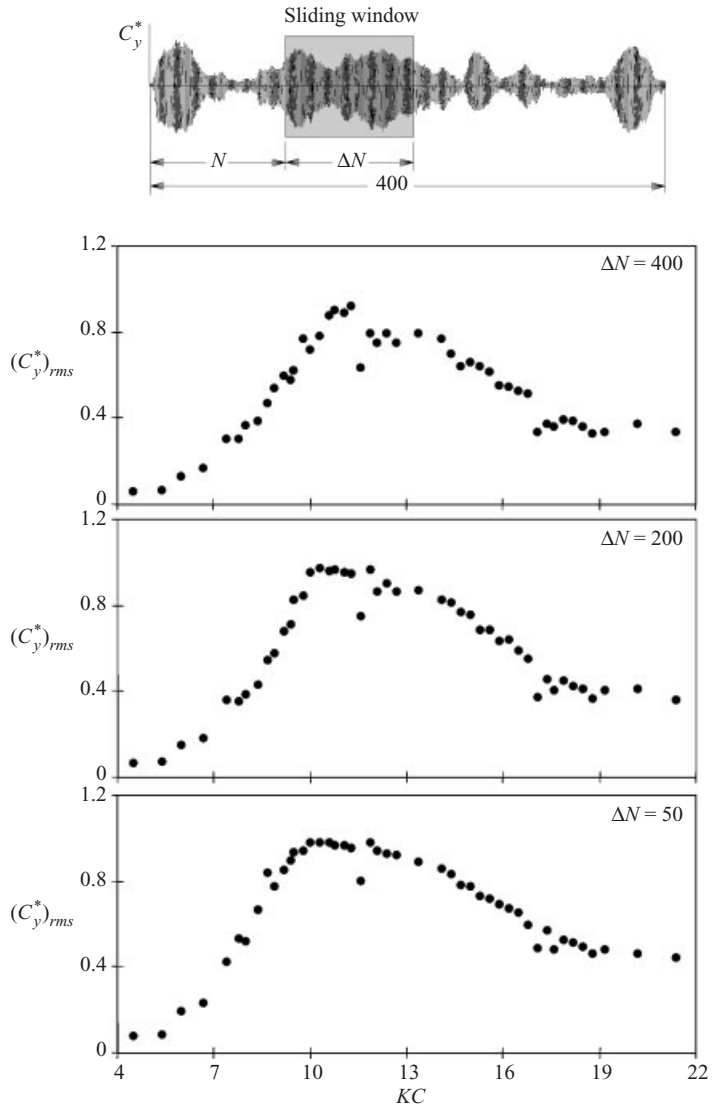


FIGURE 17. Comparison of root-mean-square value of the moment coefficient C_y^* due to the transverse force as a function of KC for various lengths ΔN of the sliding window.

figure 16. Calculation of these spectra was based upon a portion of the total record length extending over 50 oscillation cycles. The portion of the moment trace selected for evaluation was based upon a sliding window concept. A window of width $\Delta N = 50$ cycles was translated along the time axis until a maximum root-mean-square value of C_y^* was obtained. This portion of the trace was then employed for the calculation of the spectra. For $KC = 7.4$ to 15.9, there is little change in the predominant frequency, or in its harmonics and subharmonics. For all spectra, the predominant spectral component is at $f/f_w = 2$, in which f_w is the frequency of the wave. It is evident that these spectra do not adequately reflect the severe amplitude modulation effects, which are represented by the probability density distributions of figure 15.

The effect of a sliding window of several lengths $\Delta N = 50$, 200 and 400 on the

https://doi.org/10.1017/S0022112002008133 Published online by Cambridge University Press

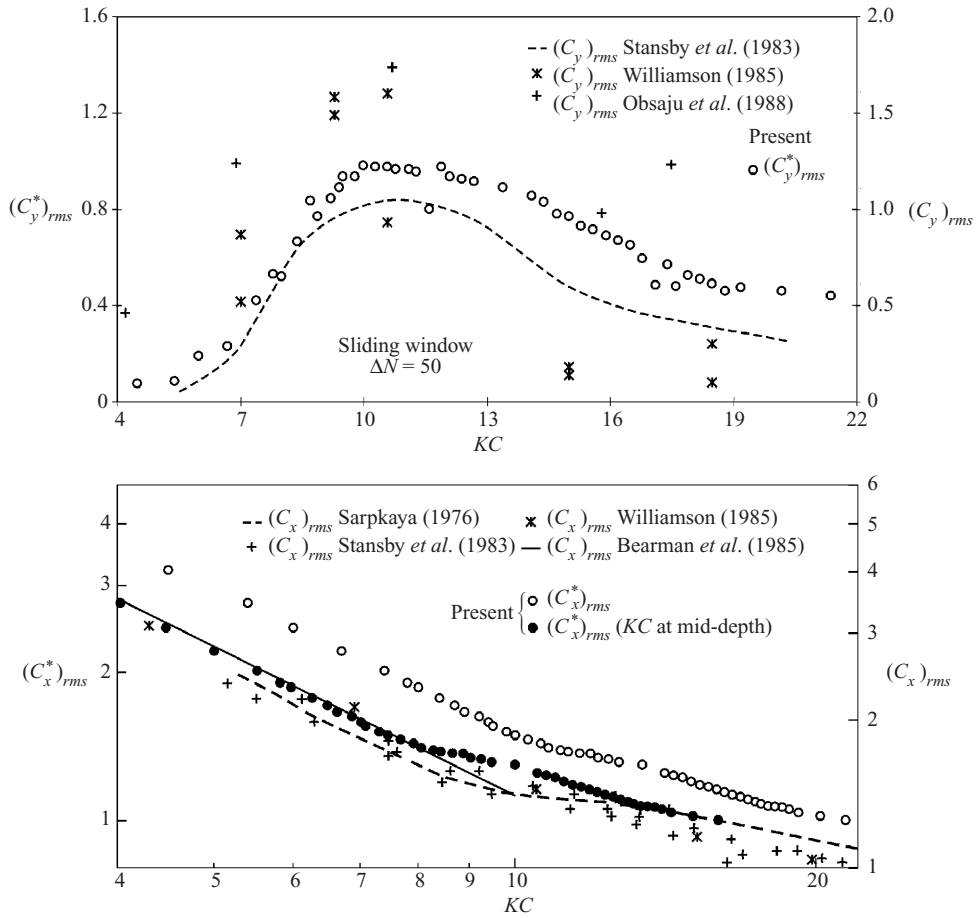


FIGURE 18. Comparison of root-mean-square values of the moment coefficient C_y^* due to the transverse force and moment coefficient C_x^* due to the in-line force with previous results of the transverse force coefficient C_y and in-line force coefficient C_x as a function of KC. A direct comparison can be made between the variations of the dimensionless moment coefficients $(C_y^*)_{rms}$, $(C_x^*)_{rms}$ and the force coefficients $(C_y)_{rms}$, $(C_x)_{rms}$. If, as an approximation, the resultant force is taken to act at the mid-depth of the submerged cylinder, then the right-hand scale of each plot corresponds to the force coefficients $(C_y)_{rms}$ and $(C_x)_{rms}$ associated with the moment coefficients $(C_y^*)_{rms}$ and $(C_x^*)_{rms}$.

root-mean-square values of C_y^*, i.e. $(C_y^*)_{rms}$, is shown in figure 17. At each value of ΔN only that portion of the time trace yielding the maximum value of $(C_y^*)_{rms}$ was plotted as a data point in each of the plots of figure 17. The effect of decreasing the length ΔN of a sliding window is to smooth the distributions of $(C_y^*)_{rms}$ versus KC. For all cases, however, the peak value occurs at or in the vicinity of $KC = 10$. The magnitude of this peak value is largest for $\Delta N = 50$ but does not depart significantly from the peak values for $\Delta N = 200$ and 400.

Plots of the root-mean-square values of transverse and in-line force coefficients, as well as the moment coefficients due to transverse and in-line forces, are given in figure 18. The symbols $(C_y)_{rms}$ and $(C_x)_{rms}$ represent the r.m.s. values of the transverse and in-line coefficients respectively for unidirectional oscillations of flow past a stationary cylinder (Williamson 1985; Obasaju *et al.* 1988; Sarpkaya 1976), as

https://doi.org/10.1017/S0022112002008133 Published online by Cambridge University Press

well as for a wave past a stationary cylinder (Stansby *et al.* 1983). For the present data, $(C_y^*)_{rms}$ and $(C_x^*)_{rms}$ are the root-mean-square values of the moment coefficients due to the transverse and in-line forces, which are defined in § 2. Unlike the case of unidirectional oscillatory flow, the magnitude of the effective unsteady velocity U varies with depth. It is taken as the horizontal projection of the orbital velocity. For the data of the present study, a sliding window of $\Delta N = 50$ was applied to the time trace of C_y^* at each value of KC. This distribution is compared with the data of Williamson (1985) and Obasaju *et al.* (1988) for unidirectional oscillatory flow past the cylinder, as well as with Stansby *et al.* (1983) for a wave of wavenumber $kd = 0.77$ past the cylinder. All distributions of $(C_y)_{rms}$ and $(C_y^*)_{rms}$ have a generally similar form with a peak near $KC = 10$.

Justensen (1989) and Bearman *et al.* (1985) provide data for the variation of the transverse force coefficient $(C_y)_{rms}$ with KC, but at values of Reynolds number $Re = KC\beta$ much larger than those of the present investigation. Nevertheless, peak values occur in the vicinity of $KC = 10$.

Corresponding values of the moment coefficient $(C_x^*)_{rms}$ due to the in-line force are compared in figure 18 with the force coefficients $(C_x)_{rms}$ of Williamson (1985), Bearman *et al.* (1985), and Sarpkaya (1976) (transformed by Stansby 1983) for unidirectional oscillatory flow past a stationary cylinder, as well as with the data of Stansby *et al.* (1983), who correlated data for $(C_x)_{rms}$ versus KC for various values of an orbital parameter Ω of a wave interaction with a vertical cylinder. The data presented here correspond to their smallest value of orbital parameter $\Omega = 0.3$. For the present data, the hollow and filled symbols represent respectively the values of KC evaluated at the free surface and mid-depth. The agreement of the overall form of the $(C_x^*)_{rms}$ distributions with previous investigations of the force coefficients $(C_x)_{rms}$ suggests that the time-averaged effects of the spanwise modes of three-dimensional vortex formation from the cylinder do not appear to significantly influence the magnitude of $(C_x^*)_{rms}$.

For both plots of figure 18, a direct comparison can be made between the variations of the dimensionless moment coefficients $(C_y^*)_{rms}$, $(C_x^*)_{rms}$, and the force coefficients $(C_y)_{rms}$, $(C_x)_{rms}$. If, as an approximation, the resultant force is taken to act at the mid-depth of the submerged cylinder, then the right-hand scale of each plot corresponds to the force coefficients $(C_y)_{rms}$ and $(C_x)_{rms}$ associated with the moment coefficients $(C_y^*)_{rms}$ and $(C_x^*)_{rms}$.

7. Concluding remarks

The spanwise modes of three-dimensional flow structure have been characterized for the case of a vertical, stationary cylinder in a free surface wave. The incident wave is a generic one; it exhibits an elliptical particle trajectory at the free surface and a unidirectional, oscillatory trajectory at the bottom of the wave tank. The modes are interpreted in terms of patterns of instantaneous velocity and vorticity, and for selected cases, they are referenced to the instantaneous moment coefficients C_y^* and C_x^* due to transverse and in-line forces respectively.

Instantaneous velocity fields, more specifically contours of constant horizontal (crossflow) velocity along the cylinder, provide a basis for defining the basic spanwise modes. The possible modes are defined in terms of zero crossings of these velocity contours, which, in turn, lead to definition of a spanwise wavelength λ. This interpretation is complemented by, and is consistent with, modes defined using contours of constant streamwise vorticity. The spanwise modes are broadly classified on the

https://doi.org/10.1017/S0022112002008133 Published online by Cambridge University Press

basis of Keulegan–Carpenter number KC, which, in turn, is an indication of the wave amplitude. At relatively low $KC = 4.5$, relatively small-scale spanwise modes can arise. The wavelength of the spanwise mode is the same as the wavelength between concentrations of streamwise vorticity.

For the range of moderate KC, which includes $KC = 10$ and 18 as representative cases, large-scale spanwise modes can occur. Their wavelengths can be one to two orders of magnitude larger than the wavelength between relatively small-scale streamwise vorticity concentrations that are embedded in a given large-scale mode.

Irrespective of the value of KC, however, the spanwise modes can be generally classified as sinuous S and unidirectional U. For the sinuous mode, the overall form of the instantaneous velocity field as well as the alternating arrangement of contours of constant transverse (horizontal) velocity exhibit a sinusoidal-like variation along the span of the cylinder. On the other hand, for the unidirectional mode, the field of velocity vectors is biased in a preferential direction along the entire span of the cylinder, and the contours of constant transverse (horizontal) velocity component correspond to a unidirectional component along the entire span. Furthermore, the large-scale features of the arrangements of streamwise vorticity contours can also be employed to arrive at the same general classification of sinuous and unidirectional modes.

In the following, the distinctive features of the three-dimensional modes along the span of the cylinder at low and moderate values of KC are summarized, then the loading on the cylinder is assessed.

7.1. *Small-scale modes along the span of the cylinder at low KC*

The well-known three-dimensional instability at low KC, originally addressed by Honji (1981), has been characterized in detail for the case of an oscillating cylinder in quiescent fluid, as summarized in § 1.

For the present case of a wave past a stationary cylinder, this instability is also evident at a relatively low value of $KC = 4.5$. The spanwise wavelength of the instability λ relative to the cylinder diameter D, λ/D, scales with the ratio of the minor B to major A axes of the orbital motion of the wave, i.e. B/A. Near the free surface, the value of λ/D can be as high as 4.5, and near the bottom (solid) surface of the wave tank where the oscillatory flow is unidirectional, $\lambda/D \approx 1$. In the present investigation, these spanwise modes are interpreted in terms of fields of instantaneous velocity vectors, contours of constant horizontal velocity and contours of constant streamwise vorticity ω_x. The specific form of each of these modes is found to be a function of the instantaneous location of the wave trough and crest relative to the position of the cylinder. Furthermore, for locations immediately beneath the free surface, more than one admissible mode of three-dimensionality can occur. That is, both sinuous and unidirectional modes are possible.

On the other hand, at locations sufficiently far beneath the free surface, the modes are consistently of the sinuous type. Apparently, in this region, the combination of a lower value of KC, as well as a low value of B/A, promotes consistency of a given mode.

Irrespective of whether one considers the region immediately beneath, or further below, the free surface, it is important to distinguish between representations of a given three-dimensional, spanwise mode based on modes of velocity versus vorticity. Although the effective wavelength of the three-dimensional spanwise mode, i.e. λ/D, is essentially the same for contours of constant horizontal velocity and contours of constant streamwise vorticity, the details are distinctly different.

https://doi.org/10.1017/S0022112002008133 Published online by Cambridge University Press

7.2. *Moderate and large-scale modes along the span of the cylinder at moderate values of KC*

A well-known feature of this moderate range of $KC = 10$ to 18 is the generation of locally, two-dimensional, staggered patterns of large-scale (ω_z) vortices in the near wake of the cylinder. The consequence of this pronounced vortex formation is to sweep fluid in the transverse direction across the face of the cylinder. In contrast, at the low values of KC addressed in the previous section, smaller-scale vortices, which tend to form in a symmetrical pattern, remain in the immediate proximity of the cylinder. This distinct difference in the nature of the locally two-dimensional vortex formation influences the relationship between the wavelength of the spanwise modes and the wavelength between individual concentrations of streamwise vorticity ω_x. In fact, the spanwise modes described at low KC in the previous section are the same, while the modes summarized in this section can be an order of magnitude larger.

The first type of mode has a 'sinuous' form and is designated as mode S. That is, the field of instantaneous velocity exhibits a sinusoidal-like variation with depth, which corresponds to a number of zero crossings of the horizontal component of velocity along the span of the cylinder. Additional types of sinusoidal S modes correspond to a smaller number of zero crossings of the horizontal velocity component along the span of the cylinder, and thereby larger values of spanwise wavelength up to two orders of magnitude larger than the cylinder diameter. All of the admissible spanwise modes have been correlated with time traces of the moment coefficient $C_y^*(t)$ due to the transverse force. Those modes that have two or more zero crossings yield very low peak values of $C_y^*(t)$.

The limiting spanwise mode corresponds to unidirectional deflection of the entire near wake region along the span of the cylinder at a given instant, i.e. the unidirectional mode U. Remarkably, this unidirectional mode can occur for values of KC as high as 18, despite the large-amplitude orbital motion of the wave near the free surface and the substantial gradient of the orbital parameter B/A with increasing depth from the free surface. These unidirectional modes yield, of course, the maximum values of the peak moment coefficient C_y^* due to the transverse force.

A further interpretation of these spanwise modes involves contours of constant streamwise vorticity ω_x. For the sinuous S mode, the overall arrangement of the small-scale vorticity concentrations shows large-scale, sinuous distortions that are highly correlated to the S modes based on velocity. Embedded within this large-scale distortion are small-scale concentrations of streamwise vorticity with a spanwise spacing much smaller than the wavelength of the large-scale mode. For the unidirectional U mode, the overall arrangement of the streamwise vorticity concentrations does not exhibit large-scale spanwise undulations, and it is again well-correlated to the U mode based on velocity. The small-scale concentrations of streamwise vorticity of the U mode still have, however, a relatively small spanwise spacing. Furthermore, irrespective of whether the S or U mode occurs, the concentrations of streamwise vorticity are arranged in an orderly, contiguous pattern over the lower region of the cylinder, where the wave motion is essentially unidirectional and has a lower amplitude than near the free surface. On the other hand, near the free surface, more complex clusters of small-scale vorticity concentrations exist.

7.3. *Loading of the cylinder*

The admissible modes along the span of the cylinder at moderate values of KC, as summarized in § 7.2, have been correlated with the instantaneous traces of the moment coefficient C_y^* due to the transverse force. When two or more zero crossings

https://doi.org/10.1017/S0022112002008133 Published online by Cambridge University Press

of the transverse velocity component occur in the near wake, the peak values of C_y^* are barely detectable and, as the limit of unidirectional motion of the near wake is approached, the peak values of C_y^* attain their maximum values. In contrast, the admissible spanwise modes of three-dimensionality have a relatively minor effect on the overall form and peak values of the moment coefficient C_x^* due to the in-line force. A phase-referenced comparison of the instantaneous traces of C_x^* for various spanwise modes shows that local distortions at and near the peaks of C_x^* can occur, and the particular type of local distortion is a function of the mode of the spanwise three-dimensionality.

As summarized in the § 7.2, the spanwise modes exhibit a number of forms, each having a different number of zero crossings and thereby a different magnitude of the peak value of the moment coefficient C_y^* due to the transverse force. These instantaneous values of C_y^*, when considered over a relatively long time span, generally exhibit substantial amplitude modulation. This modulation arises from the spontaneous transition from one type of mode to another. The degree of amplitude modulation for a long-time record of $C_y^*(t)$ has been characterized as a function of KC. A type of probability density function is shown to be effective in representing the major features of the strongly modulated moment traces. On the other hand, if a sliding window concept is employed to sample the portion of the amplitude-modulated trace of $C_y^*(t)$ that has the largest root-mean-square value, it is possible to show that the classical, one-dimensional spectra of C_y^* can exhibit remarkably similar forms over a range of KC.

The root-mean-square values of the moment coefficient due to the transverse force are compared with those of transverse force coefficient from previous investigations of both unidirectional oscillatory flow and a free surface wave past a stationary cylinder, as summarized in §§ 1 and 6. A universal observation is that the maximum values of those coefficients occur at or near $KC = 10$, irrespective of the type of unsteady flow past the cylinder. The present investigation shows that this maximum r.m.s. moment is associated with minimal amplitude modulation of the corresponding moment trace and persistence of the unidirectional spanwise mode U over a large number of wave cycles. The implication is that the particular mode of locally two-dimensional vortex formation at or near $KC = 10$ is compatible with the robust spanwise mode of the unidirectional type, i.e. mode U.

The overall form of the curves representing the root-mean-square values of the moment coefficient C_x^* due to the in-line force, in particular the manner in which they vary with KC, agree well with data for the in-line force coefficient from previous investigations involving unidirectional motion. This observation indicates that the time-averaged values of C_x^*, are relatively insensitive to the form of the instantaneous spanwise mode, in agreement with the aforementioned features of the timewise variation of C_x^*.

The authors are pleased to acknowledge financial support from the Office of Naval Research under Grant N00014-94-1-0815, P00001, monitored by Dr Thomas Swean. Supplemental support was provided by the Office of Naval Research Grant N00014-99-1-0581, as well as by NSF Grant CTS-9803734, monitored by Dr Roger Arndt and Dr John Foss.

REFERENCES

Bearman, P. W., Chaplin, J. R., Graham, J. M. R., Kostense, J. K., Hall, P. F. & Klopman, G. 1985 The loading on a cylinder in post-critical flow beneath periodic and random waves. *Proc. 4th Intl Conf. on Behaviour of Offshore Structures, Delft* (ed. J. A. Battjes). Developments in Marine Technology, vol. 2, pp. 213–225. Elsevier.

https://doi.org/10.1017/S0022112002008133 Published online by Cambridge University Press

Bearman, P. W., Graham, J. M. R., Naylor, P. & Obasaju,, E. D. 1981 The role of vortices in oscillatory flow about bluff cylinders. *Intl Symp. on Hydrodynamics and Ocean Engng*, pp. 621–644. The Norwegian Institute of Technology.

Bearman, P. W., Graham, J. M. R. & Obasaju, E. D. 1984 A model equation for the transverse forces on cylinders in oscillatory flows. *Appl. Ocean Res.* **6**, 166–172.

Chakrabarti, S. K. 1980 In-line forces on a fixed vertical cylinder in waves. *J. Waterway, Port, Coastal Ocean Division, ASCE* **106**, 134–155.

Dean, R. G., Dalrymple, R. A. & Hudspeth, R. T. 1981 Force coefficients from wave projects i and ii. Data including free-surface effects. *Soc. Petrol. Engrs J.* December, 777–786.

Dütsch, H. L. 2000 Numerische simulation mechanischer fluid-struktur-wechselwirkungen bei großen auslenkungen. PhD Dissertation, University of Erlangen, Nürnberg.

Dütsch, H., Durst, F., Becker, S. & Lienhart, H. 1998*a* Low-Reynolds-number flow around an oscillating circular cylinder at low Keulegan–Carpenter numbers. *J. Fluid Mech.* **360**, 249–271.

Dütsch, H., Durst, F. & Brenner, G. 1998*b* Three-dimensional vorticity structure in the flow around an oscillating circular cylinder at low Reynolds and Keulegan–Carpenter numbers. *Proc. 1998 Conf. on Bluff Body Wakes and Vortex-Induced Vibration* (ed. P. W. Bearman & C. H. K. Williamson). 1998 ASME Fluids Engng. Div. Annual Summer Meeting, Washington, DC, 21–25 June.

Elston, J., Blackburn, H. M. & Sheridan, J. 2000 The onset of three-dimensionality in the flow generation by an oscillating circular cylinder. *Bull. Am. Phys. Soc. 53rd Ann. Mtg. of Div. Fluid Dynamics, November 19–21, Washington, DC*, vol. 45, pp. 21.

Honji, H. 1981 Streaked flow around an oscillating circular cylinder. *J. Fluid Mech.* **107**, 509–520.

Ikeda, S. & Yamamoto, Y. 1981 Transverse force forces on cylinders in oscillatory flows. *Rep. Dept. Foundation of Engng. and Coastal Engng, Saitama University, Japan*, vol. 10, pp. 1–16.

Ippen, A. T. 1966 *Estuary and Coastline Hydrodynamics.* McGraw-Hill.

Iwagaki, Y., Asano, T. & Nagai, F. 1983 Hydrodynamic forces on a circular cylinder placed in wave-current co-existing fields. *Memo Fac. Engng, Kyoto University, Japan* **45**, 11–23.

Justensen, P. 1989 Hydrodynamic forces on large cylinders in oscillatory flow. *J. Waterway, Port, Coastal Ocean Engng* **115**, 497–514.

Kozakiewicz, A., Sumer, B. M. & Fredsøe, J. 1992 Spanwise correlation on a vibrating cylinder near a wall in oscillatory flows. *J. Fluids Struct.* **6**, 371–392.

Lighthill, J. 1978 *Waves in Fluids.* Cambridge University Press.

Lin, J.-C. & Rockwell, D. 1999 Horizontal oscillations of a cylinder beneath a free-surface: vortex formation and loading. *J. Fluid Mech.* **389**, 1–26.

Obasaju, E. D., Bearman, P. W. & Graham, J. M. R. 1988 A study of forces, circulation, vortex modes around a circular cylinder and oscillating flow. *J. Fluid Mech.* **196**, 467–494.

Ramberg, S. E. & Niedzwecki, J. M. 1979 Some uncertainties and errors in wave force computations. *Proc. 11th Offshore Technology Conf., Houston*, vol. 3, pp. 2091–2101.

Rockwell, D., Lin, J.-C., Cetiner, O., Downes, K. & Yang, Y. 2001 Quantitative imaging of the wake of a cylinder in a steady current and a wave. *J. Fluids Struct.* **15**, 427–444.

Sarpkaya, T. 1976 Vortex shedding and resistance in harmonic flow about smooth and rough circular cylinders at high Reynolds numbers. *Naval Postgraduate School, NPS*, 59SL 76021, Monterey, CA.

Sarpkaya, T. 1984 Discussion of quasi 2-d forces on a vertical cylinder in waves (paper No. 17671 by P. K. Stansby *et al.*). *J. Waterway, Port, Coastal Ocean Engng* **110**, 120–123.

Sarpkaya, T. 1986 Force on a circular cylinder in viscous oscillatory flow at low Keulegan–Carpenter numbers. *J. Fluid Mech.* **165**, 61–71.

Sarpkaya, T. & Isaacson, M. 1981 *Mechanics of Wave Forces on Offshore Structures.* Van Nostrand Reinhold.

Singh, S. 1979 Forces on bodies in oscillatory flow. PhD Thesis, University of London.

Stansby, P. K. 1976 The locking-on of vortex shedding due to the cross-stream vibration of circular cylinders in uniform and shear flows. *J. Fluid Mech.* **74**, 641–655.

Stansby, P. K., Bullock, G. N. & Short, I. 1983 Quasi-two-dimensional forces on a vertical cylinder in waves. *J. Waterway, Port, Coastal Ocean Engng* **109**, 128–132.

Sumer, B. M. & Fredsøe, J. 1997 *Hydrodynamics Around Cylindrical Structures.* World Scientific.

Tatsuno, M. & Bearman, P. W. 1990 A visual study of the flow around an oscillating circular

https://doi.org/10.1017/S0022112002008133 Published online by Cambridge University Press

cylinder at low Keulegan–Carpenter numbers and low stokes numbers. *J. Fluid Mech.* **211**, 157–182.

TØRUM, A. 1989 Wave forces on pile in surface zone. *J. Waterway, Port, Coastal Ocean Engng* **115**, 547–565.

WILLIAMSON, C. H. K. 1985 Sinusoidal flow relative to circular cylinder. *J. Fluid Mech.* **155**, 141–174.

https://doi.org/10.1017/S0022112002008133 Published online by Cambridge University Press